Fabrication and Characterization of Iron Oxide Thin Films Prepared By the Thermal Oxidation of Iron

BY

Muhammad Saleem

A Thesis Presented to the

DEANSHIP OF GRADUATE STUDIES

KING FAHD UNIVERSITY OF PETROLEUM & MINERALS

DHAHRAN, SAUDI ARABIA

In Partial Fulfillment of the
Requirements for the Degree of

MASTER OF SCIENCE

In

PHYSICS

April, 2012

KING FAHD UNIVERSITY OF PETROLEUM & MINERALS
DHAHRAN 31261, SAUDI ARABIA

DEANSHIP OF GRADUATE STUDIES

This thesis, written by **Muhammad Saleem** under the direction of his thesis advisor and approved by his thesis committee, has been presented to and accepted by the Dean of Graduate Studies, in partial fulfillment of the requirements for the degree of **MASTER OF SCIENCE IN PHYSICS**.

Thesis Committee

Advisor
Prof. Mohammad F. Al-Kuhaili

Co-advisor
Prof. Sardar Mohammad Ayub

Member
Prof. Khalil A. Ziq

Member
Prof. Nouar Tabet

Member
Prof. Akhtar A. Naqvi

Department Chairman
Dr. Abdul-Aziz Al-Jalal

Dean of Graduate Studies
Dr. Salam A. Zummo

22/5/12
Date

عمادة الدراسات العليا
DEANSHIP OF GRADUATE STUDIES

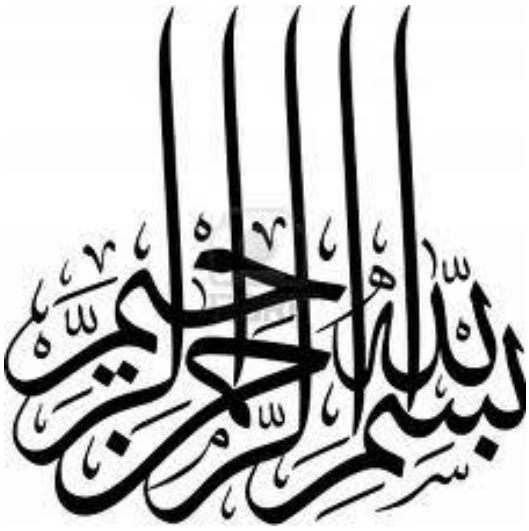

"It is better to speak to a seeker of knowledge than to remain silent, but silence is better than idle words"

Prophet Muhammad (peace be upon him)

Dedicated to My Parents, Wife, Brothers, Sisters and Teachers

ACKNOWLEDGEMENT

Thanks to Almighty Allah who gave me the courage to accomplish this work successfully. Peace and blessings of Almighty Allah be upon beloved Prophet Muhammad.

I would like to acknowledge the all kind of supports of King Fahd University of Petroleum & Minerals for successful completion of my graduate studies in Physics Department. I am also thankful to the chairman and all staff members of the Physics Department for their support and cooperation.

I would especially like to thank and appreciate the support and supervision of my thesis advisor Prof. Mohammad Al-Kuhaili. My heartfelt gratitude goes to him for his excellent cooperation, encouragement and technical guidance throughout the work. It was my great honor to work with such a nice, helpful and kind person. I am also thankful to him for devoting and sparing his precious time for this work and the things he taught me. His skills, knowledge and guidance will definitely help me in future.

I am also very thankful to my co-advisor Prof. Sardar Mohammad Ayub for his technical assistance during the experiments. I would like to appreciate his moral support, motivation and useful discussions during this work.

Special thanks are also due to my committee members Prof. Nouar Tabet, Prof. Khalil A. Ziq and Prof. Akhtar A. Naqvi for their useful comments, discussions and encouragements. Their suggestions are appreciated.

I would like to thank Dr. Muhammad Baseer Haider for his fruitful suggestions.

My deep appreciation goes to Prof. Ibrahim Nasser and Dr. F. Z. Khiari for their moral support and invaluable advice throughout my studies and research.

I would like to appreciate the help and cooperation of Mr. Imran Bakhtiari. I am thankful to him for his support throughout my research in thin film lab.

I would like to thank all my friends in the Physics Department and all my friends at Student Housing for their encouragement and moral support during my stay for graduate program.

Finally, I want to give my very special appreciation to my parents, brothers and sisters for their patience, encouragement, support and prayers throughout my M.S. program. I am very thankful to my wife for her love, support, encouragement and sacrifice.

TABLE OF CONTENTS

LIST OF FIGURES

LIST OF TABLES

ABSTRACT

Name: Muhammad Saleem

Title: Fabrication and characterization of iron oxide thin films prepared by the thermal oxidation of iron

Major Field: Physics

Date of degree: April, 2012

Iron oxide thin films were deposited by electron beam (e-beam) evaporation from pure iron. Two types of evaporation were done. Firstly, iron was deposited in vacuum, and secondly, the reactive evaporation of iron was carried out in an oxygen atmosphere. Films were post-annealed in air in the temperature range 200 ^{o}C to 500 ^{o}C. The structural properties were investigated by X-ray diffraction, revealed the growth of α-Fe_2O_3 (hematite). The films were polycrystalline with nanocrystallite size. The chemical properties of the films were determined from X-ray photoelectron spectroscopy, and highly reactive nature of iron oxide films was elucidated. The surface morphological properties of the films were determined using atomic force microscopy. The surface roughness and lateral mean grain size of the films were increased with annealing. The optical properties of the films, including the refractive index, extinction coefficient, absorption coefficient, and band gap were determined from spectrophotometric measurements. Films were highly transparent and exhibited high values of refractive indices. All the films had direct as well as indirect band gaps. The direct band gap values were 2.21 ± 0.03 eV and indirect band gap values were 1.98 ± 0.02 eV.

ABSTRACT (ARABIC)

ملخص الرسالة

الاســــــــــم: محمد سليم

عنوان الرسالة : تحضير ودراسة طبقات رقيقة من أكسيد الحديد بواسطة الأكسدة الحرارية للحديد

مجال التخصص: فيزيـــاء

تاريخ التخرج : إبريل 2012

يناقش هذا البحث تحضير طبقات رقيقة من أكسيد الحديد بواسطة تبخير الحديد بأشعة الإلكترونات. و قد تم تحضير الطبقات بطريقتين: الأولى تمثلت في تبخير الحديد في وسط مشبع بالأكسجين على طبقات مسخنة و غير مسخنة ، و الثانية هي تبخير الحديد في و سط مفرغ من الهواء و من ثم أكسدته عن طريق تسخينه في الهواء في درجات حرارة من 200 إلى 500 درجة مئوية. الخصائص التركيبية للطبقات أوضحت أنها تتكون من أكسيد الحديد الثلاثي (α-Fe_2O_3) و أنها ذات تركيب متعدد البلورة. و بالإضافة لذلك، فإن التحليل الكيميائي أكد درجة التفاعل الكبيرة للحديد مع الأكسجين. خصائص السطوح تمت دراستها بواسطة مجهر القوة الذرية ، حيث وجد أن درجة الخشونة و حجم البلورات يتناسبان طريا مع ارتفاع درجة الحرارة. من الناحية الضوئية تمت دراسة معامل الانكسار و معامل الامتصاص و طاقة الفجوة، حيث تبين أن هذه الطبقات تتميز بمعاملات انكسار كبيرة و أنها شفافة.

CHAPTER 1

Introduction

The study of metal oxides is significantly important in many scientific disciplines like physics, chemistry, and materials science and engineering as far as fundamental studies and technological applications are concerned. There are many scientific issues that can be addressed, and applications that can be benefit from the study of these compounds. Iron oxide belongs to the family of transition metal oxides and has found important applications in various scientific and technological fields.

1.1 PROPERTIES OF IRON OXIDES

The known iron oxides are FeO (Wüstite), Fe_3O_4 (Magnetite), α-Fe_2O_3 (Hematite), γ-Fe_2O_3 (Maghemite), β-Fe_2O_3 and ε-Fe_2O_3 [1–4]. These oxides exhibit different properties and stability due to which each oxide is important for research and certain applications. These oxides can transform into each other, depending on the growth conditions and growth techniques. A brief introduction to each of these oxides is given below.

1.1.1 Wüstite

Wüstite is the phase of iron oxide which contains divalent cations (Fe^{2+}). It has black color, with the chemical formula FeO, and known as ferrous oxide. It is one of the rare iron oxide and an important intermediate during the iron ores reduction. It has cubic rock salt like structure with lattice constant a = 0.4302 – 0.4275 nm [1,5]. In its crystal structure, O^{2-} anions form a cubic close packed face-centered cubic (fcc) sublattice with Fe^{2+} cations located in the octahedral interstitials [6].

1.1.2 Magnetite

This oxide is also of black color, and exists in nature as a mineral magnetite. It contains both Fe^{2+} and Fe^{3+} ions. It is also named as ferric oxide, and is formulated as Fe_3O_4. It has a cubic inverse spinel structure with lattice constant $a = 0.8396$ nm [1]. Its structure consists of cubic O^{2-} anions that form a cubic closed packed sublattice, with the tetrahedral interstitials occupied by Fe^{3+} cations and octahedral interstitials occupied by same numbers of Fe^{2+} and Fe^{3+} cations [6]. It is a ferrimagnet with a high Curie temperature about 585 ^{o}C, and is electronically conducting with highly spin-polarized conduction electrons [7]. Therefore, it is an interesting candidate for magnetic recording media or spin valve applications [8]. It has also drawn a great deal of interest for tunneling magnetoresistance (TMR) devices [5].

1.1.3 Hematite

Hematite is the oldest known iron oxide, generally with red-blood color which is abundantly found in rocks and soils. It is written as α-Fe_2O_3 and has a hexagonal corundum (α-Al_2O_3) structure with lattice constants a = 0.50353 – 0.5034 nm and c = 1.37495 – 1.3752 nm [1,9]. In its crystal structure, O^{2-} anions form a hexagonal close

packed (hcp) sub lattice, while Fe^{3+} cations are distributed in the octahedral interstitials. It is the most stable phase of iron oxide, and therefore is the final oxide during the transformation from other iron oxides. Hematite is an antiferromagnetic material with a Neel temperature of 677 ^{o}C below the Morin transition at -13.15 ^{o}C, but shows ferromagnetic and paramagnetic natures at high temperatures [10].

Hematite is very important as a prototype candidate due to its technological uses as a catalyst [11,12] and photocatalyst [13]. Due to low cost and high stability and intermediate band gap, this material has shown a great interest for solar energy conversion applications. Additionally, there has been a great interest in the potential use of hematite in low cost processes to photocatalytically split water for hydrogen production [14,15]. It has been found broad range of applications due to its chemical stability and semiconducting properties such as humidity sensors and α-Fe_2O_3 doped with quadrivalent metal ions such as Si, Zr, Ti and Sn has been found to be sensitive to combustible gases [16,17]. It is also very important for alkaline batteries, electro-chromic, and as a dielectric in microelectronic devices [18–22]. Because of its high refractive index and high absorption at short wavelengths, it is suitable for optical interface filters, especially long-wave pass filters [22].

1.1.4 Maghemite

Maghemite is formulated as γ-Fe_2O_3 and it is a metastable phase at ambient conditions, but transforms into α-Fe_2O_3 when heated above 400 ^{o}C [23]. Maghemite is a ferrimagnetic material and has a cubic inverse spinel structure similar to magnetite with saturation magnetization of 390 kA/m [24,25]. However, it exists with Fe^{2+} deficiency and has lattice constant a = 0.83474 nm [1,26].

γ-Fe_2O_3 films are routinely incorporated in high-density magnetic recording devices [27]. It is also a material of interest due its applications as a gas sensitive material [28], and catalysis [29]. It is also a promising candidate for integrated inductors and for microwave application due to its low conductivity, high saturation magnetization and high Curie temperature above room temperature [30].

1.1.5 β-Fe_2O_3

This phase of iron oxide does not exist naturally. However it has been synthesized in laboratory. It is also metastable and coverts into α-Fe_2O_3 at temperature above 500 ^oC [31]. It has a body centered cubic (bcc) structure with lattice constant a = 0.9398 nm [32].

1.1.6 ε- Fe_2O_3

This oxide has also been claimed only in laboratory so far. It is metastable and transforms to the α-Fe_2O_3 phase between 500 and 750 °C. Its structure is intermediate between the α- and the γ- phases. However, it has an orthorhombic structure with lattice constants a = 0.5095 nm, b = 0.879 nm, and c = 0.9437 nm [1]. It is ferromagnetic with a Curie temperature of 750 °C [33].

1.2 LITERATURE REVIEW

Due to the numerous applications of iron oxide thin films, various approaches have been explored to fabricate and characterize these materials. It should be noted that the experimental technique is one factor along with other factors, like growth mode, growth parameters, and post deposition treatment that influence the properties and structure of

the films. We will now consider the major deposition techniques that have been utilized in the deposition of iron oxide thin films.

1.2.1 Spray Pyrolysis Technique

Goyal *et al*. [34] reported the effect of substrate temperature (T_s) ranging from 400 ^{o}C to 700 ^{o}C on iron oxide thin films grown on quartz substrates. They noticed the transformation of amorphous to crystalline structure of magnetite films at 500 ^{o}C. The films grown at 600 ^{o}C were exhibiting magnetite as well hematite phase. However, films were completely transformed into hematite phase at 700 ^{o}C.

The influence of substrate temperature from 350 ^{o}C to 500 ^{o}C and growth time was investigated by A. A. Akl [19]. The amorphous α-Fe_2O_3 was fabricated at 350 ^{o}C but well polycrystalline rhombohedral phase of α-Fe_2O_3 was obtained for T_s > 350 ^{o}C. The longer growth time also made it possible to fabricate polycrystalline structure. The films had porous island structure and had significantly larger grain size.

The doping of iron oxide by different type of elements is very important in certain applications. Stable Al-doped α-Fe_2O_3 thin films revealed the presence of an oxygen deficiency, and exhibited n-type conductivity, as was reported by Shinde *et al.* [18]. The presence of aluminum also enabled the increase of the direct band gap from 2.2 to 2.25 eV. The grain size was also increased at some optimized doping concentration.

Well crystallized α-Fe_2O_3 thin films were obtained from amorphous films after annealing them in vacuum for temperatures ranging 250 – 400 ^{o}C, as reported by Ouertani *et al.* [35]. The films were compact with granular structure and the average crystallite size was increased from 45 nm to 85 nm with increasing the annealing temperature. They also found that the films were exhibiting direct band gap values about 2.1 eV.

1.2.2 Chemical Vapor Deposition

Pure and Sn-doped α-Fe_2O_3 thin films were fabricated by plasma enhanced chemical vapor deposition (PECVD) by Lee *et al*. [17]. The films were deposited on Al_2O_3 substrates at various deposition temperatures up to 300 ^oC. Porous films with polycrystalline structure having about 10 nm crystallite size were obtained which are indeed suitable for gas sensing application. The films were found to be highly sensitive for i-C_4H_{10} and CO gases but not for CH_4 gas. It was observed that the post heat treatment at 550 ^oC and 650 ^oC improved the gas sensitivity.

Thin films of iron oxide were also synthesized by K. Shalini *et al.* [36] using metal-organic chemical vapor deposition (MOCVD) on fused quartz substrates. The pure polycrystalline Fe_3O_4 phase was obtained for substrate temperatures ranging 475−550 ^oC, however there was a co-existence of α-Fe_2O_3 phase above 550 ^oC. It was also investigated that high oxygen partial pressure favors the formation of α-Fe_2O_3. The band gap of α-Fe_2O_3 (2.2 eV) is larger than band gap of Fe_3O_4 (0.5 eV). Therefore, α-Fe_2O_3 films were more transparent than Fe_3O_4 films. The grain size and surface morphology were changed, which also confirmed the phase transformation with increasing substrate temperature.

M. K. Singh *et al.* [37] studied the temperature dependence of the growth rate of iron oxide thin films deposited on Si (100) substrate using metal-organic chemical vapor deposition (MOCVD). The growth rates were studied in the temperate range of 400 – 600 ^oC. The polycrystalline structure of pure α-Fe_2O_3 phase was found. The shape and size of crystallites was also influenced by the growth temperature.

1.2.3 Pulsed Laser Deposition

Maghemite thin films with either single crystal or with large oriented polysrystals, with common in-plane directions on MgO substrate were reported by Tepper *et al.* [38]. Iron oxide thin films were deposited by pulsed laser deposition (PLD). The influence of laser fluency on thickness and the correlation between film thickness and roughness of the films were also investigated. The obtained films were very smooth and uniform and their magnetic and optical properties were also determined. They found that absorption is lower in films deposited under a small oxygen pressure.

In PLD, there are several experimental factors which can change the properties of thin films. Ouyang *et al.* [39] studied these experimental factors which included the laser energy, growth in vacuum, reactive environment and substrate temperature with ferric methacrylate as the source target. Iron rich Fe_2O_3 and α-Fe_2O_3 phases were obtained.

Experimentally, it is possible to achieve two different phases using the same growth method with similar substrate and at constant temperature but with different ambient pressures. Shima *et al.* [40] fabricated iron oxide films with various growth temperatures and oxygen partial pressure on Si (001) substrate using PLD. α-Fe_2O_3 phase was obtained in oxygen ambient while γ-Fe_2O_3 phase was obtained under vacuum conditions at a growth temperature of 400 ^{o}C, along with polycrystalline structure. γ-Fe_2O_3 showed saturation magnetization very close to bulk γ-Fe_2O_3. However, it was inversely related to film thickness. The films consisting of α-Fe_2O_3 also showed ferromagnetic behavior.

1.2.4 Sputtering

FeO thin films grown from Fe_3O_4 target using ion beam sputtering on Si (001) substrates under oxygen ambient, were investigated by Kim *et al.* [4]. They studied the effect of

post annealing and substrate temperature on the films. The films of Fe_3O_4 were polycrystalline at room temperature. However nanocrystalline Fe phase was present at a substrate temperature of 300 ^oC, along with the Fe_3O_4 phase. Phase transformation to highly oriented FeO (200) was achieved by post-annealing at 600 ^oC. Initially the surfaces of the films were flat but were significantly roughened for high substrate temperatures.

Polycrystalline hematite thin films deposited by DC reactive magnetron sputtering from 99.95% pure Fe as a target, were reported by Miller *et al.* [21]. Thin films were grown under various conditions of oxygen partial pressure and at substrate temperature up to 200 ^oC. The crystallite size was found to be increased with growth temperature, and was decreased with oxygen partial pressure. The growth on heated substrates promoted the mobility, and hence the conductivity, due to reduced inter-grain scattering for large crystallites. Both direct and indirect band gaps $1.95 - 2.01$ eV and $2.14 - 2.2$ eV respectively, were reported and the size of the crystallites was correlated with the band gap.

1.2.5 Epitaxial Growth

Multilayer growths of iron oxide thin films have many advantages in magnetic applications. In order to improve the magnetic properties of the films, epitaxial growth is desirable. The studies of surface and interface properties of iron oxide thin films on foreign single crystal substrate are very important. Ruby *et al.* [41] studied the surface and interface properties of iron oxide thin films on MgO (001) substrates. The growth was done using molecular beam epitaxiay (MBE) under ultra high vacuum conditions. Fe_3O_4 (001) thin films with 5 nm and 25 nm thicknesses were prepared and were

annealed in dry air at 400 − 600 K. The phase transformation from Fe_3O_4 to γ- Fe_2O_3 was observed at 500 K. The interdiffusion of magnesium and iron, and modification in chemical environment of magnesium was observed for low film thickness at higher temperatures.

Hasegawa *et al.* [42] investigated the electrical and magnetic properties of γ- Fe_2O_3 (001) epitaxial films deposited MgO (001) substrates using ozone-assisted molecular beam epitaxy method. The resistivity of the films was found to be temperature-dependent and was as high as ~10^2 Ω.cm. The cubic and uniaxial anisotropy constants were found. The decrease in the cubic anisotropy constant was supposed to be due to surface and lattice strain effects.

Waddill *et al.* [43] investigated the growth mode of epitaxial iron oxide films on Ag (111) grown by two different methods. In the first growth method, iron films with a thickness of 1−10 monolayers were deposited and then oxidized. The poorly-ordered Fe (110) structure was transformed into poorly-ordered FeO (111) structure after the oxidation. The second deposition was the sequential deposition of Fe films followed by oxidation, which resulted in crystalline FeO (111) growth. However, the thicker films were containing Fe_3O_4 (111) phase.

1.2.6 Evaporation

Aronnimei *et al.* [44] deposited iron oxide thin films from gas-phase on a glass substrates. They found γ- Fe_2O_3 at a growth temperature of 350 ^oC, whereas α- Fe_2O_3 was found at higher growth temperatures. The grain size was observed to increase between 350 ^oC and 450 ^oC. It was also observed that by increasing the deposition time, the films were grown with Fe ions in divalent state.

Iron ultra-thin films were prepared by thermal evaporation of a high purity Fe by Corneille *et al.* [45]. The films were deposited on Mo (100) substrate in the 100 – 1500 K substrate temperature range. Iron oxide films were obtained from post-oxidation and in situ oxidation. The XPS results showed the phase changes for the thermal reduction of the Fe_2O_3 to Fe_3O_4 at ~550 K and Fe_3O_4 to FeO at ~750 K.

High refractive index and high absorption at short wavelength of iron oxide thin films are highly desirable. Park *et al.* [22] investigated the optical and structural properties of Fe_2O_3 thin films. The films were deposited by conventional electron-beam evaporation and ion-beam assisted deposition (IBAD) on glass substrates and silicon wafers. The post annealing of the films improved the crystallite size and roughness of the films.

Fujii *et al.* [46] analyzed the formation ranges of different phases of iron oxide. They deposited the iron oxide films using thermal evaporation of high purity iron metal on sapphire (0001). It was observed that the oxidation degree of deposited iron oxides is dependent on oxygen partial pressure, substrate temperature and kind of substrates. From their results they generated the phase diagram for the formation of various phases of iron oxide under different conditions like substrate temperature and oxygen partial pressure. It was noticed that films thicker that 20 nm had Fe_3O_4 while γ- Fe_2O_3 was obtained for films thickness lower than 20 nm.

Chiba *et al.* [47] prepared the ferrite ($FeO\text{-}Fe_2O_3$) thin films by electron beam evaporation of iron ingot on glass substrates. α-Fe_2O_3 was obtained by heating the iron films in an infrared oven at 400 ^oC for 120 min. Fe_3O_4 was prepared from the deposition of iron on α-Fe_2O_3 films and was annealed at 400 ^oC. Films were polycrystalline and the

effect of heating rates on the formation of Fe_3O_4 was investigated. Furthermore, the magnetic properties like saturation magnetization and coercive force were obtained.

The interface properties of Fe_2O_3 were investigated by Jain *et al.* [48]. Thin films were grown using an electron beam evaporation technique from a pure Fe_2O_3 target on Si (001) substrates. Al and Cu buffer layers were used for interface properties and were explained on the basis of enthalpy of formation. They found that for the films deposited directly on Si substrates and on Al buffer layer, different phases of oxides SiO_2 and Al_2O_3 were formed because the enthalpy of formation of these oxides is lower than the Fe_2O_3 phase. There were no other oxides when the films were deposited onto a Cu buffer layer because the enthalpy of formation for CuO is greater than Fe_2O_3.

Ultra thin films (4−6 nm) of FeO and Fe_3O_4 were deposited on Mg (100) substrates by thermal evaporation of pure iron. Ruby *et al.* [49] studied the structure and chemical stability of iron oxide against annealing temperatures from 300 – 1100 K. Wustite was found to be very unstable phase and was preserved as a thin film for very short time. The transformation of wustite into magnetite was noticed even at room temperature. The magnetite phase was observed to be stable even at high annealing temperatures. However, the traces of magnesium were detected after heating magnetite films at 700 K.

1.3 SCOPE OF WORK

A plenty of research has been done so far in order to study the iron oxides thin films under different conditions by various deposition techniques. However, the existences of multiple phases of iron oxides during the films fabrication have been a great challenge. It is a great desire to fabricate the iron oxide thin films with single phase. The aim of this work was the growth of single phase Fe_2O_3 by one of the simplest techniques, e-beam evaporation, under feasible and more practical conditions. In comparison to previous studies, our study of growth of α-Fe_2O_3 is simpler and more practical for future applications of α-Fe_2O_3. Two growth techniques, both of which are based on electron beam evaporation, were used. In the first technique, pure iron was evaporated in vacuum. Subsequently, the iron films were annealed in air to oxide them. In the second technique, iron was reactively evaporated in an oxygen atmosphere, both on heated and unheated substrates. These films were annealed in air to investigate the improvement of their oxidation upon annealing. The resulting iron oxide phases, surface morphology, and surface chemical structure were investigated. Moreover, the optical properties of the resulting films were determined.

CHAPTER 2

Experimental Techniques and Details

2.1 E-BEAM EVAPORATION

Electron beam (e-beam) evaporation is one of the most widely used thin film deposition techniques [50,51]. Figure 2.1 shows a schematic diagram of e-beam evaporation. An electron beam is thermionically emitted from a heated filament. The beam is accelerated and focused by electric and magnetic fields onto an evaporant material. The filament cathode is potential biased with a high-voltage DC power supply, typically with a voltage range of 1 to 30 kilovolts. In order to deflect the electron beam in a 270^{o} circular arc and focus it on evaporant, a transverse magnetic field is applied. When the electron beam strikes the target surface, the kinetic energy of electrons is transformed into thermal energy. Thus the surface of the material becomes molten and eventually evaporates. The evaporant holder is water cooled in order to prevent it from melting. The evaporant materials in the form of vapors travel upward and deposit on the desired substrates.

2.2 ADVANTAGES OF E-BEAM EVAPORATION

There are several advantages of e-beam evaporation over other techniques. Some of them are mentioned below.

i. It is very easy to handle and operate.

ii. It gives high purity thin films.

iii. Many samples can be prepared during a single deposition.

iv. It offers many desirable characteristics such as flexible deposition rates ranging from 1nm/minute to100 nm/minute.

v. Deposition parameters can be controlled during the thin film growth.

vi. It yields very smooth deposition.

vii. It provides strong metallurgical bonding and polycrystalline microstructure.

viii. It is capable of producing multilayered and nano-laminated metallic/ceramic coatings at relatively low temperatures.

ix. It is useful for alloys depositions and for elements with low vapor pressure.

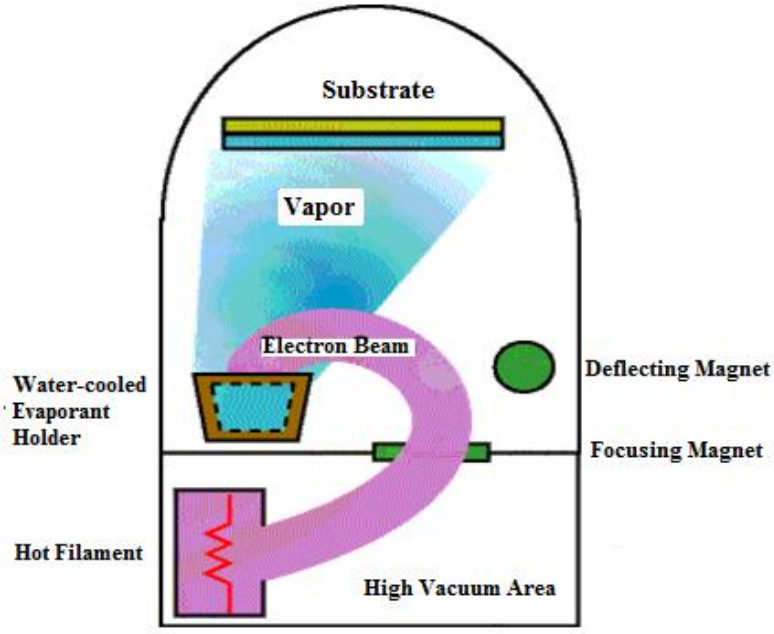

Figure 2.1. Schematic diagram of e-beam evaporation.

Figure 2.2. Leybold L560 box coater.

2.3 THIN FILM DEPOSITION AND PROCESSING

2.3.1 Thin Film Deposition

Thin film deposition was carried out by electron-beam evaporation using a 4 kW electron gun in a Leybold L560 box coater (figure 2.2) that was evacuated by a turbomolecular pump. The starting material was solid iron granules (Alfa Aesar, purity 99.999%). The material was slowly out-gassed before evaporation. The system was pumped to a base pressure of 4×10^{-4} Pa. The films were deposited on fused silica for X-ray diffraction (XRD), atomic force microscopy (AFM), and for optical measurements. Films were also deposited on tantalum substrates for X-ray photoelectron spectroscopy (XPS) analysis. The substrates were rotating during the deposition, and the source–to–substrate distance was 40 cm. The evaporation rate was set at 0.2 nm/s while the thickness of the films was controlled by a quartz crystal thickness monitor. We deposited three sets of films

i. Deposition on unheated substrates in vacuum (RW films).

ii. Deposition on unheated substrates under an oxygen partial pressure of 0.1 Pa (RO films).

iii. Deposition on heated substrates (300 ^{o}C) under an oxygen partial pressure of 0.1 Pa (HO films).

2.3.2 Annealing of the Films

After deposition, the films were annealed in a horizontal tube furnace in air in the temperature range 200 ^{o}C to 500 ^{o}C for 4 hours. After annealing, the samples were cooled down to room temperature while they were still in the furnace.

2.4 CHARACTERIZATION TECHNIQUES

Different characterization techniques were used to investigate the properties of the films. These are mentioned below.

2.4.1 Thickness Measurement

The thickness of the films was measured using a surface profilometer (Ambios XP-2). The XP2 stylus-based surface profilometer is a computerized, high-sensitivity surface profiler that measures surface flatness, curvature, roughness, waviness, and step height in a variety of applications. It has the ability to measure the step heights which is the thickness of the film from under 10 nm to as large as 400 μm precisely with an accuracy of ±5 nm without surface damage.

Working Principle: It scans the surface using the semicircular tip and records the displacement in z (vertically) direction as a function of length x (laterally). As the tip of the profilometer moves at the edge of the thin film, it measures the small variation in z direction. This change in height position (step height) generates an analogue signal which is converted into digital signal stored, analyzed and displayed. The horizontal resolution is controlled by the scan speed and scan length.

2.4.2 Structural Analysis

X-ray diffraction (XRD) is an important technique to obtain information on an atomic scale from crystalline materials. It is used to characterize the crystallographic structure, crystallite size and preferred orientation in solid samples.

Working Principle: XRD works on the basis of Bragg's law. When a monochromatic X-ray beam, with wavelength λ, is projected onto a crystalline material at an angle θ, then

the distance travelled by the rays reflected from successive planes must differ by an integer *n* of wavelengths [52].

$$n\lambda = 2d\sin\theta \qquad (2.1)$$

where *d* is spacing between the atomic planes of the sample. The schematic diagram in figure 2.3 shows the geometry of Bragg's law. The diffracted waves interfere constructively, and represent the same symmetry as in the distribution of atoms. These diffracted X-rays are then detected, processed and counted in order to deduce the distribution of atoms in the material.

The structure of our films was investigated by XRD using a Shimadzu XRD-6000 diffractometer, employing *Cu Kα* (1.54 Å) radiation. The *2θ* scan range was performed from 20^o to 80^o with *2θ* step of 0.02^o and with step acquisition time of 1.0 s.

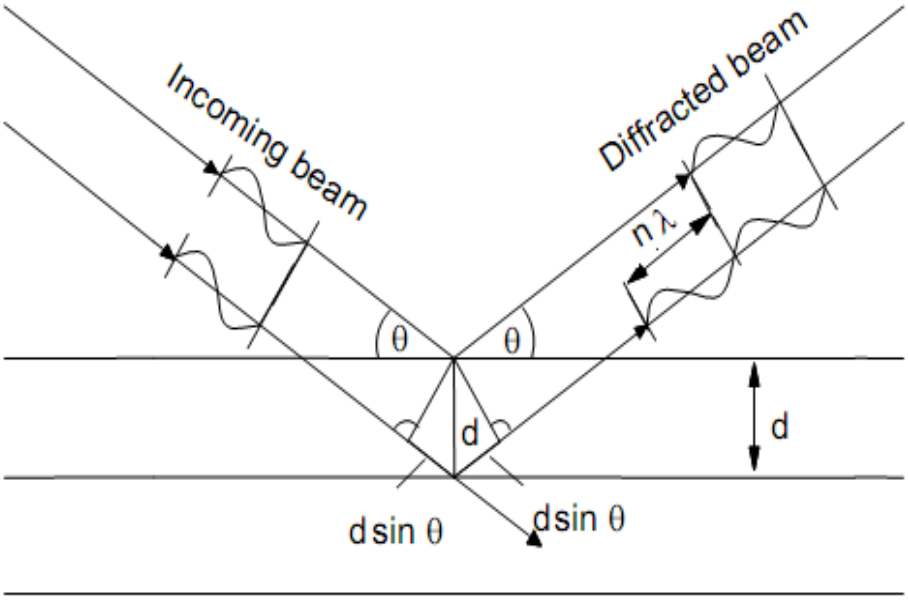

Figure 2.3. Schematic diagram of Bragg's law of diffraction.

2.4.3 Surface Morphological Analysis

Atomic force microscopy (AFM) is a high-resolution scanning probe microscopy technique, which provides resolution of the order of fractions of a nanometer of the surface of a material.

Working Principle: AFM employes a cantilever made of silicon or silicon nitride with a sharp tip (probe) of the order of nanometers at its end that is used to scan the specimen surface. When the tip is brought near to the sample surface, forces between the tip and the sample lead to a deflection of the cantilever. The forces measured by AFM are mechanical contact forces, van der Waals forces, capillary forces, bonding forces, electrostatic forces, magnetic forces, Casimir forces, and salvation forces. The deflection is measured using a laser spot reflected from the top surface of the cantilever into an array of photodiodes. A feedback mechanism is employed to adjust the tip-to-sample distance to maintain a constant force between the tip and the sample [53]. A schematic diagram of an atomic force microscope is shown in figure 2.4.

The surface morphology of our films was examined by tapping mode AFM (Veeco Innova diSPM). The sample surface was probed with a silicon tip of 10 nm radius oscillating at its resonant frequency of 300 kHz.

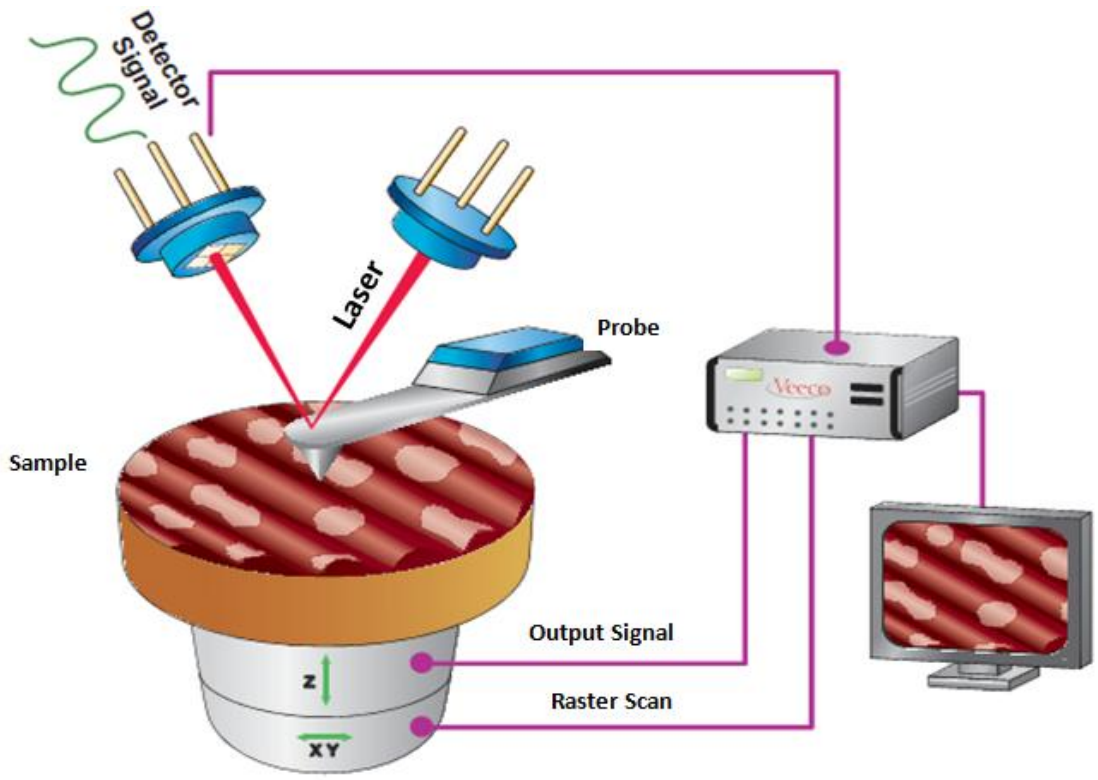

Figure 2.4. Schematic diagram of the working principle of an atomic force microscope.

2.4.4 Chemical Composition

X-ray photoelectron spectroscopy (XPS) is a surface chemical analysis technique that is used to analyze the surface chemistry of a material. It provides detailed information about the chemical composition of the surface usually down to depth of $1 - 10$ nm.

Working Principle: XPS is based on the photoelectric effect [54]. When a mono-energetic X-ray beam is directed onto the surface of the material, the energy of the X-ray photon is

absorbed by the core electrons of the atoms of the material. If the energy of the photon can knock out an electron from the atom, then the electron leaves the surface of the material with kinetic energy E_k. The emitted electron is called a photoelectron. Then the binding energy of the core electron is given by Einstein's relation:

$$h\nu = E_b + E_k + \phi \quad (2.2)$$

$$E_b = h\nu - (E_k + \phi) \quad (2.3)$$

where $h\nu$ is incident photon energy, E_b is binding energy of electron, and ϕ is the work function of the spectrometer. From the binding energy and intensity of a photoelectron peak, the elemental identity, chemical state, and quantity of an element are determined. Figure 2.5 represents a schematic diagram of the basic principle of XPS.

For our films, XPS was performed in a VG Scientific ESCALAB MKII spectrometer equipped with an Al Kα (1486.6 eV) X-ray source. Prior to the XPS analysis, the samples were transferred in air to the XPS analysis chamber. The C 1s peak of hydrocarbon contamination, at a binding energy of 284.5 eV, was used as an energy reference. During the XPS analysis, the samples were maintained at ambient temperature at a pressure of 5×10^{-7} Pa. XPS was performed on samples deposited on tantalum substrates, since the charging effects will be less for these substrates.

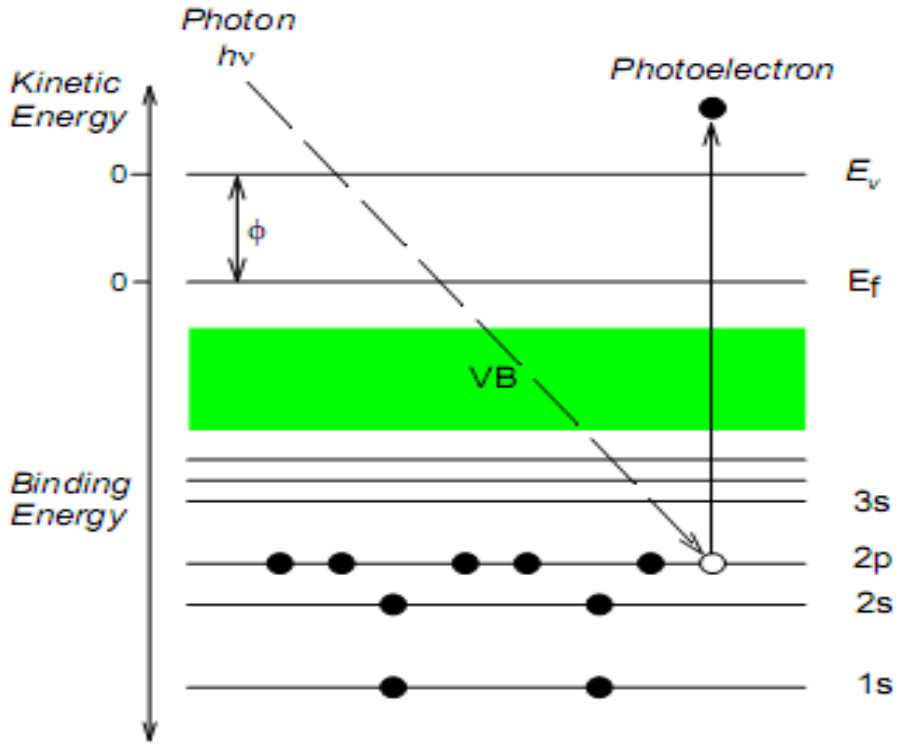

Figure 2.5. Schematic diagram of the basic principle of X-ray photoelectron spectroscopy.

2.4.5 Optical Measurements

The optical properties of a material deposited as a thin film are found by optical measurements. From these optical measurements, the information about band gap, absorption coefficient, and refractive index can be extracted. The interaction of radiation with thin films is demonstrated in a schematic diagram in figure 2.6. When the radiation interacts with the material of the thin films, a fraction *R* is reflected from the top surface of the film and a fraction *T* are transmitted through the film material. Some fraction of the

radiation is absorbed (A) by the films as well as scattered (S) at surface and volume imperfections. Adding all contributions, it is generally written as:

$$R + T + A + S = 1 \qquad (2.4)$$

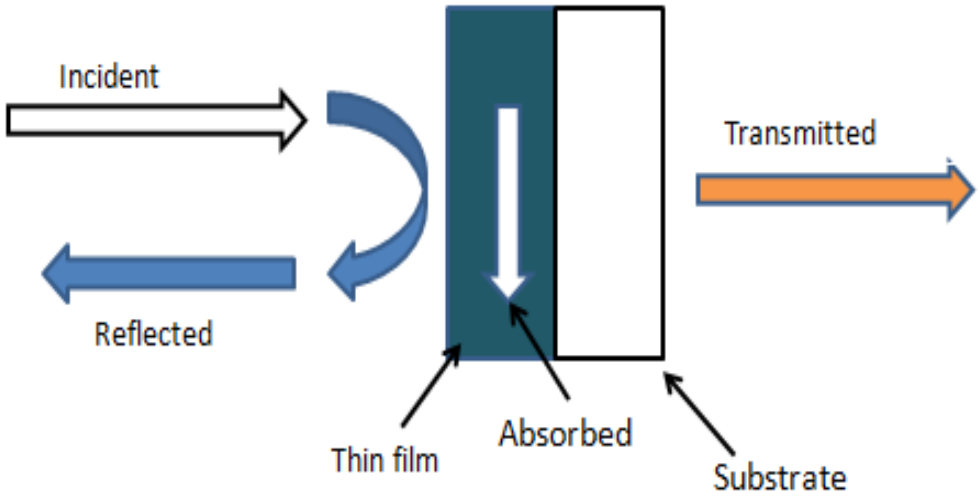

Figure 2.6. Basic principle of optical measurements of a thin film.

Normal-incidence reflectance (R) and transmittance (T) were measured over the wavelength range $200 - 1200$ nm using a Jasco V-570 double beam spectrophotometer.

Double beam spectrophotometer: A spectrophotometer is a device that is used to measure the intensity of light as a function of its wavelength. A double beam spectrometer compares the light intensity between two light paths, one path containing the reference beam and the other the test sample. Light sources, diffraction gratings, filters, photo detectors, and signal processors are the various parts of spectrophotometer.

The light source provides light with wavelength in Vis, UV, and NIR ranges. The filters and diffraction grating separate light into its component wavelengths so that very small range of wavelength can be directed onto the sample. The sample compartment permits the entry of no stray light while at the same time without blocking any light from the source. The photo detector converts the amount of light which it had received into a current which is then sent to the signal processor. The signal processor converts current into absorbance, transmittance and concentration values which are then sent to the display.

In transmission measurements the spectrophotometer quantitatively compares the amount of light that passes through the reference beam and the sample and for reflectance it compares the amount of light reflected from the reference beam and sample.

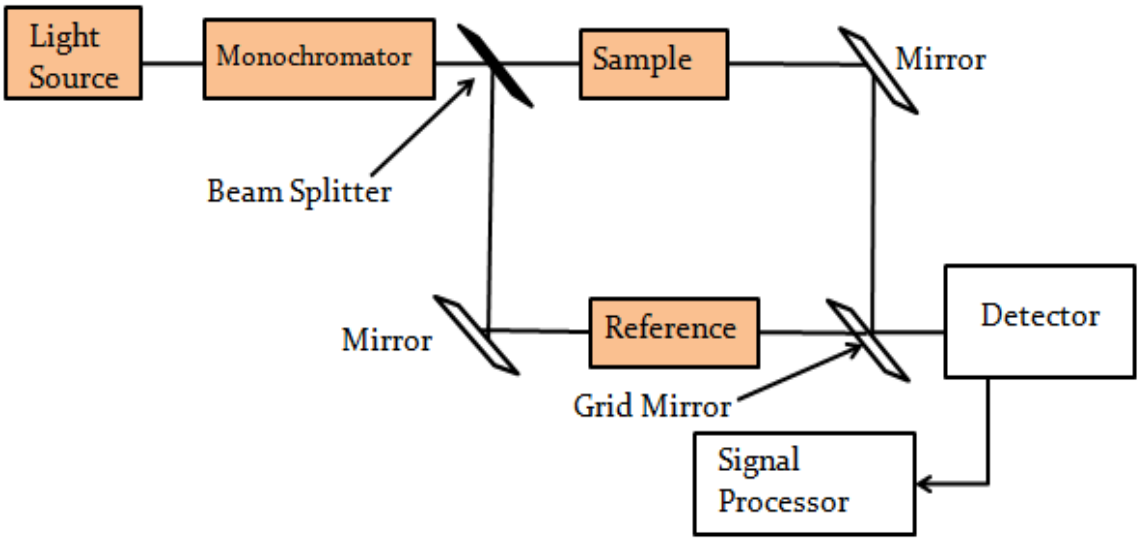

Figure 2.7. Schematic diagram of a double beam spectrophotometer.

CHAPTER 3

Structural Properties

3.1 THICKNESS MEASUREMENTS

The thickness set by the quartz crystal was 200 nm during the deposition process. However, the final thickness was measured by a stylus profilometer. The final thickness of the films was found to be different from the quartz crystal, which is due to the fact that the substrates were rotating whereas the quartz crystal was stationary. Moreover, iron has different sticking coefficients on quartz crystal as compare to fused silica. The final thickness of films deposited on unheated substrates under vacuum (RW) and films deposited on heated substrates, under oxygen ambient (HO) was less than the thickness set by quartz crystal monitor. However, the final thickness of RO films which were deposited on unheated substrates, under oxygen ambient was higher than the set thickness during the deposition. The lower thickness of the films deposited on heated substrates may be attributed to the lower sticking coefficient of the constituent elements due to substrate heating. The chemisorption of oxygen is much stronger at lower temperatures, thus the sticking probability is increased [45]

Annealing of the films also changed the final thickness of films. Figure 3.1 shows the variation of the thickness of the films as a function of annealing temperatures (T_a). The thickness of as-deposited iron films that were evaporated in vacuum (RW films) was 113 nm. This value was slightly reduced to 100 nm upon annealing at 200 ^{o}C. However, the thickness of the films was drastically increased to 220 nm when the films were annealed at 300 ^{o}C. Thereafter, the thickness of films was slightly increased to 225 nm and 229 nm at 400 ^{o}C and 500 ^{o}C, respectively. The drastic increase at 300 ^{o}C may be attributed to the onset of oxidation conformed by the XRD results. The final thickness of RO films was changed slightly upon annealing. The thickness of as-deposited RO films was 241 nm and was increased to 250 nm during annealing up to 500 ^{o}C. The thickness of HO films was 145 nm, with thickness variation less than 1% upon annealing up to 500 ^{o}C. The uncertainty in the thickness of the films was ±5 nm.

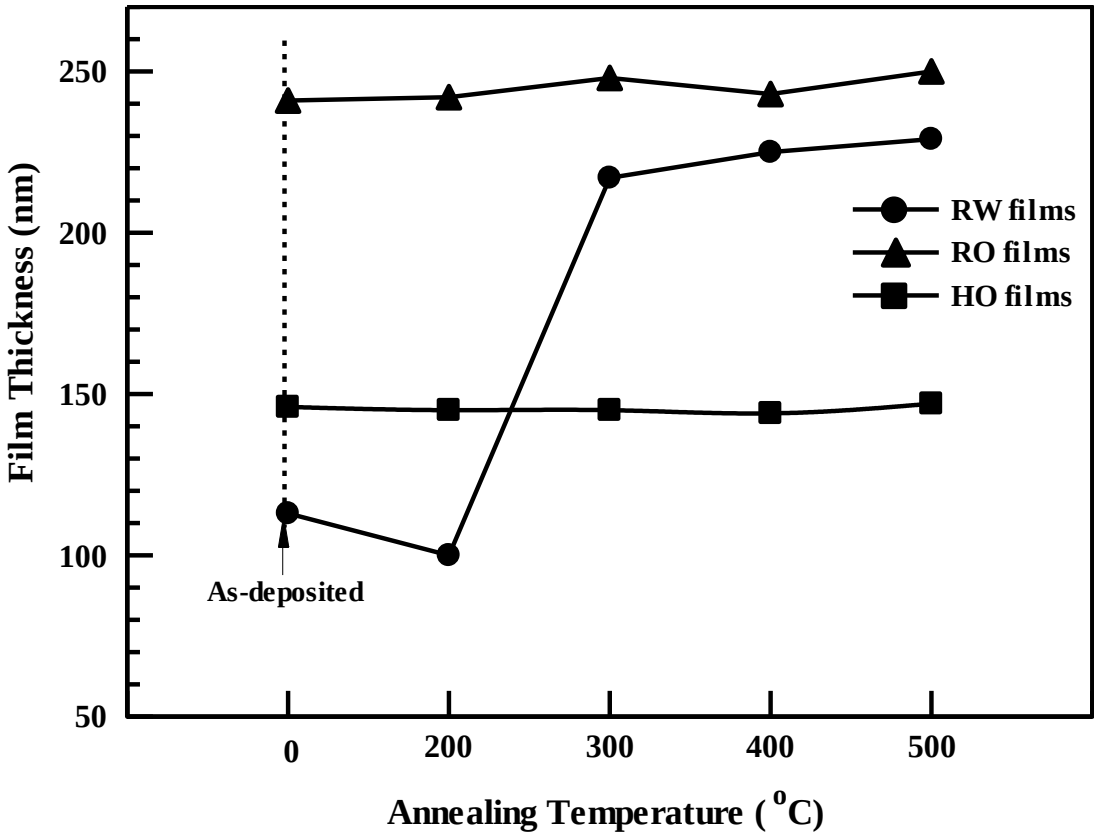

Figure 3.1. Variation in the thickness of the films with annealing temperature.

3.2 X-RAY DIFFRACTION (XRD) ANALYSIS

The XRD patterns of the films deposited under different experimental conditions and post annealed at various temperatures are shown in figures 3.2, 3.3, and 3.4. All the films exhibited the polycrystalline structure. Identification of material phases and peak assignments were based on data from the International Center for Diffraction Data (ICDD) [55]. Figure 3.2 shows the effect of annealing on RW films. The as-deposited films indicated the presence of pure elemental iron, with cubic structure with preferred orientation along (110) direction. The same behavior was observed when the films were annealed at 200 ^{o}C. There was no trace of iron oxide within the detection limit of XRD at this annealing temperature. However, the films showed the formation of iron oxide at annealing temperature of 300 ^{o}C. The films obtained the α-Fe_2O_3 phase along with pure iron. This indicates the onset of oxidation at this annealing temperature. Complete oxidation was achieved at 400 ^{o}C, where no traces of elemental iron were observed. The films showed similar behavior while annealing at 500 ^{o}C. The α-Fe_2O_3 phase was obtained after complete oxidation without any trace of elemental iron or any other phase of iron oxides. The most dominant growth was along the (104) direction. Figure 3.3 shows the XRD patterns of RO films which were reactively evaporated films on unheated substrates. No peaks due to elemental iron were detected, indicating complete oxidation of the as-deposited films. Annealing of these films up to 500 ^{o}C did not affect either polycrystallinity or the phase of iron oxide. All peaks belonged to the α-Fe_2O_3 phase with dominant growth orientation along (110) direction according to ICDD files. The XRD results of HO films that were reactively evaporated films on heated substrates are shown in figure 3.4. The preferred growth direction was along the (104) and (110) directions.

Annealing of the films did not change the polycrystallinity or phase of the material. However, HO films exhibited more polycrystalline structure than RO films. This is because of the fact that substrate heating enhances the diffusion of atoms adsorbed on the substrate, and accelerates the migration of the atoms to energy favorable positions, resulting in the enhancement of the crystallinity [56].

The average crystallite size D of the films were estimated by using the Scherrer's equation[18,57]:

$$D = \frac{0.9\,\lambda}{\beta\,cos\theta} \qquad (3.1)$$

where λ is the wavelength of X-ray, β is the full width at half maximum of the peak, and θ is the diffraction angle corresponding to that peak.

The most intense peak in every XRD pattern was used to calculate the crystallite size. The calculated crystallite sizes D are given in Table 3.1. The crystallite size of RW films was the lowest. However with the formation of iron oxide, the size of crystallites was increased. The crystallite size did not change significantly for the reactively evaporated films. The crystallite size of RO films was 14.5 ± 0.4 nm at different annealing temperatures. The HO films also showed very small variation in the crystallite size which was 14.7 ± 0.2 nm very similar to the RO films. These crystallite sizes reflect the nano-crystalline nature of films.

There are several factors that influence the crystallinity of thin films like (i) deposition technique, (ii) substrate nature (iii) substrate temperature, (iv) deposition rate, (v) oxygen partial pressure, and (vi) annealing temperature, atmosphere, and heating rate. Therefore, it is not unusual to find widely scattered results on the crystalline structure of thin films of a given material. However, our XRD results are consistent with the previous studies on

iron oxide thin films. Chiba *et al.* [47] also reported the growth of polycrystalline iron oxide thin films fabricated by e-beam evaporation of pure iron. The pure iron films were transformed to α-Fe_2O_3 with (110) dominant orientation upon heating at 400 ^oC. The effect of deposition under an oxygen atmosphere was investigated by Fujii *et al.*[46]**.** Their results showed that more oxidized phases were obtained at low substrate temperatures and high oxygen partial pressure. The phase diagram for the formation of iron oxides as a function of the substrate temperature and oxygen partial pressure is shown in figure 3.5. In our results, the formation of α-Fe_2O_3 phase is consistent with the phase diagram.

Table 3.1. Crystallite size as calculated from XRD spectra.

T_a (^oC)	Crystallite size (nm)		
	RW films	**RO films**	**HO films**
As	10.2	14.1	15.0
200	10.2	14.5	14.6
300	13.3	14.9	14.9
400	14.9	14.5	14.5
500	14.4	14.6	14.6

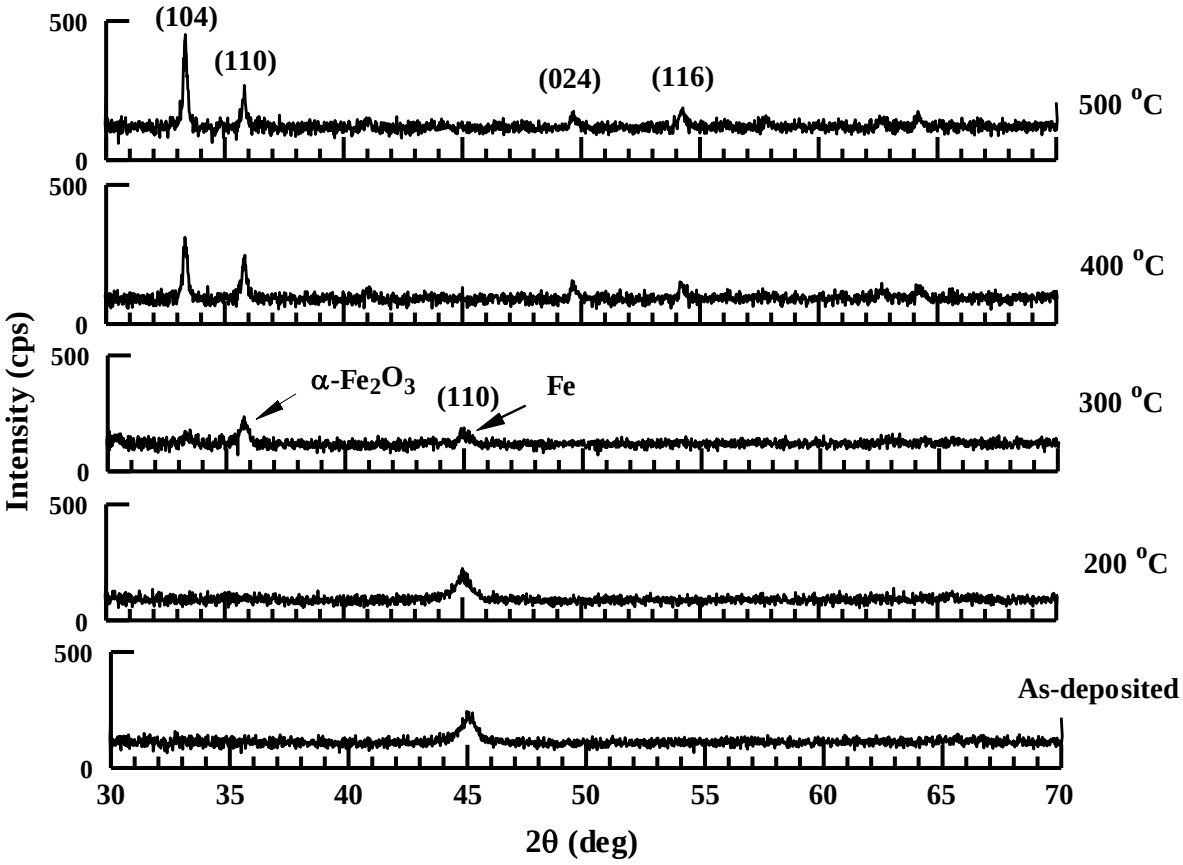

Figure 3.2. XRD patterns of the films deposited on unheated substrates in vacuum (RW films), and annealed in air at the temperatures indicated on the figures.

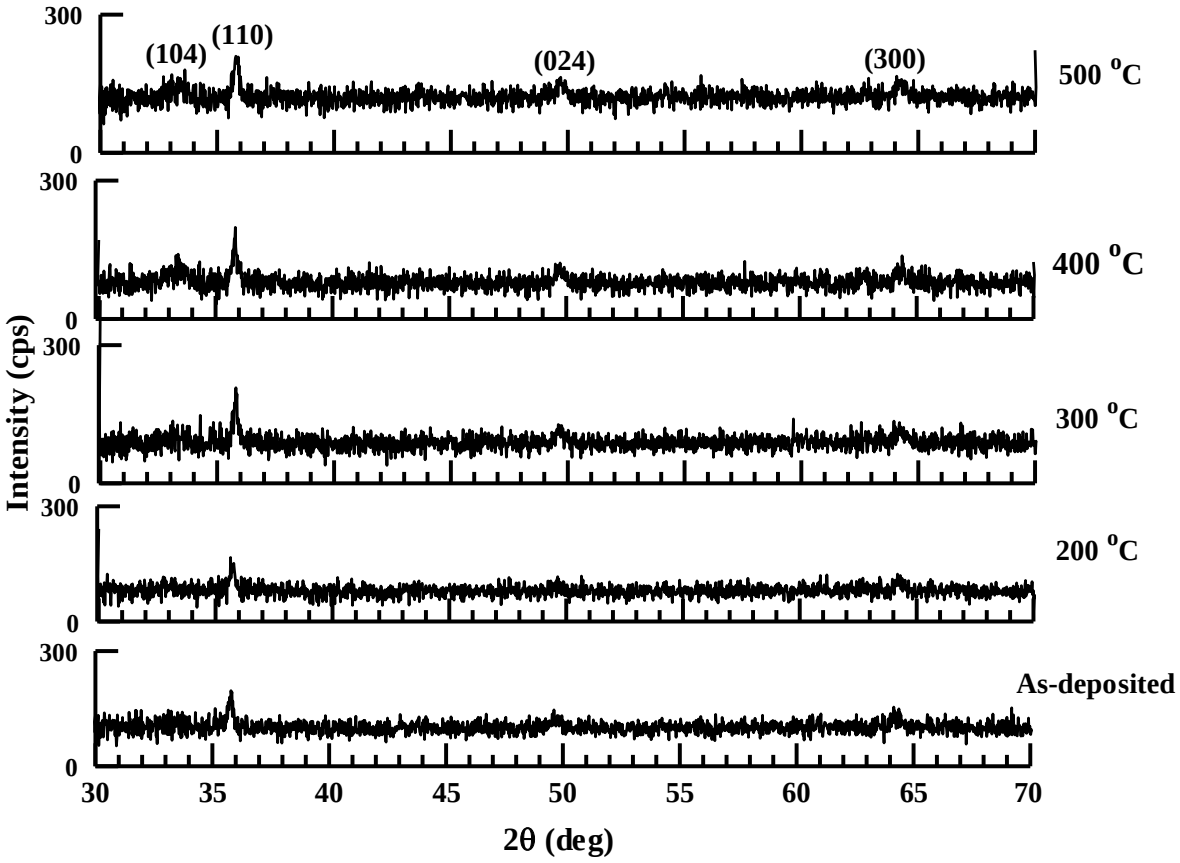

Figure 3.3. XRD patterns of the films deposited on unheated substrates in oxygen (RO films), and annealed in air at the temperatures indicated on figures.

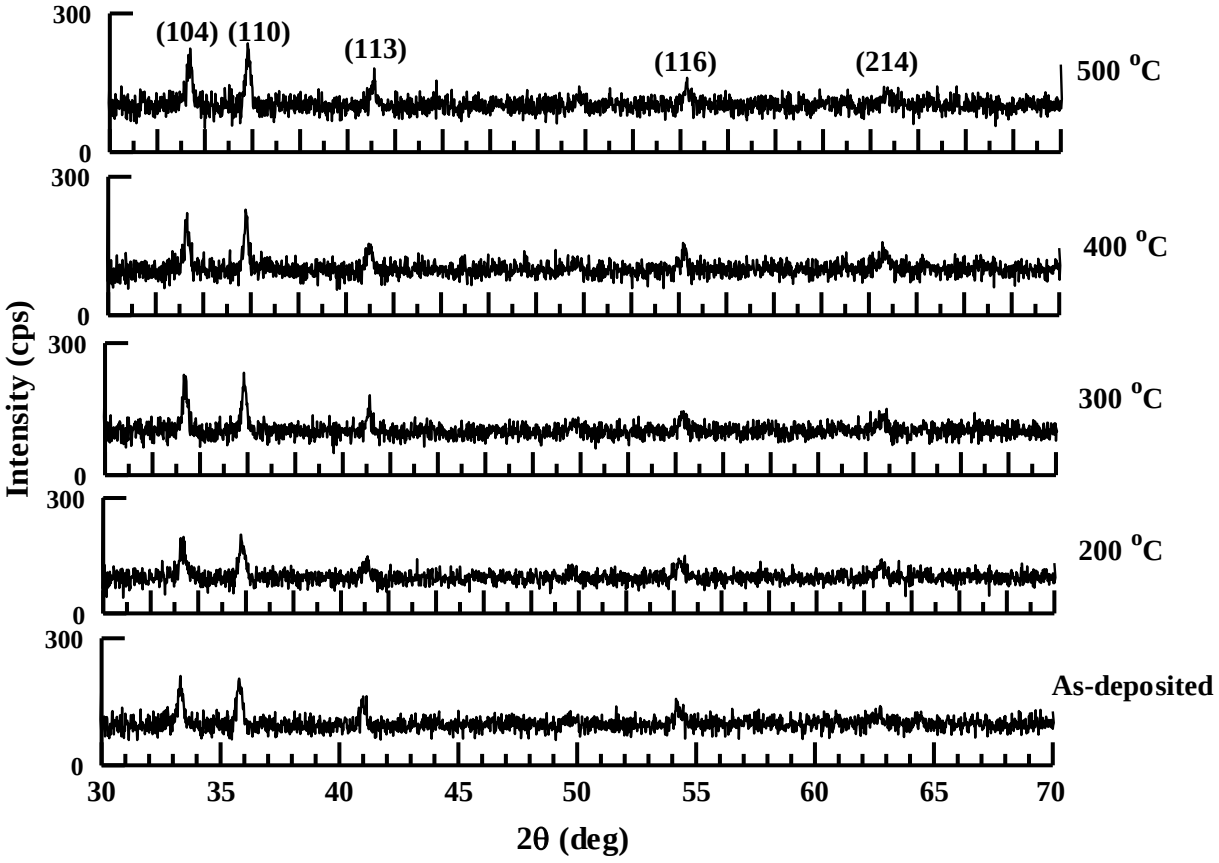

Figure 3.4. XRD patterns of the films deposited on heated substrates in oxygen (HO films), and annealed in air at the temperatures indicated on figures.

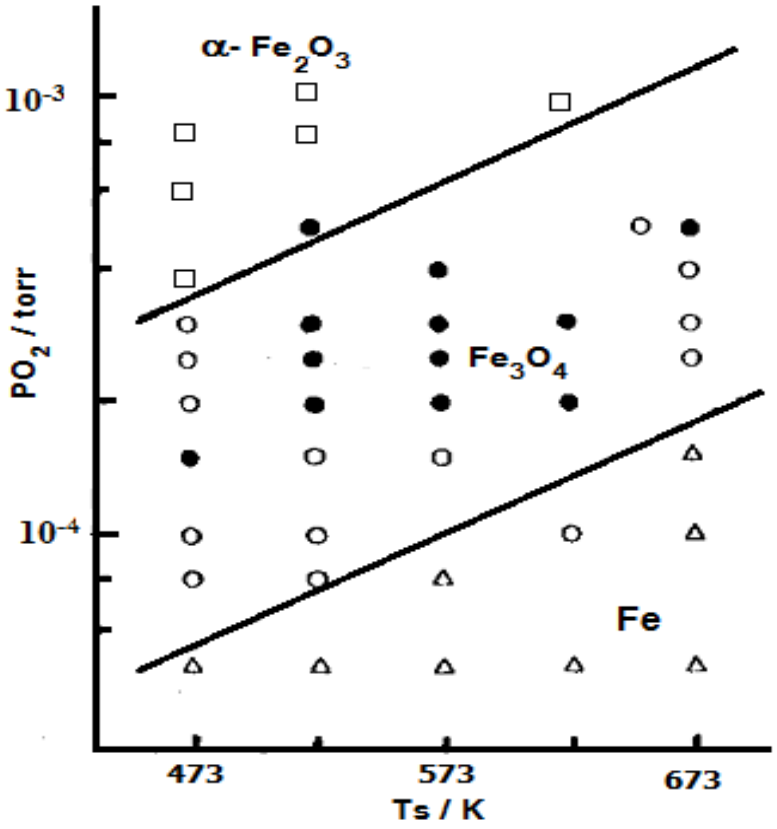

Figure 3.5. Phase diagram for Fe, Fe_3O_4 and α-Fe_2O_3 as functions of substrate temperature (T_s) and oxygen partial pressure P_{O2}. Ref.[46]. △: (110) - oriented Fe metal, ○ : randomly oriented Fe_3O_4, ● : (111)- oriented Fe_3O_4, □ : (0001)- oriented α-Fe_2O_3.

3.3 MORPHOLOGICAL ANALYSIS

AFM was used to characterize the surface morphology of the films, and to estimate the surface root-mean-square roughness (R_{rms}) and the lateral (surface) grain size. Figure 3.6 shows the three dimensional AFM images of films deposited in vacuum on unheated substrates (RW films). The morphology of the as-deposited films was characterized by irregular grains with an R_{rms} value of 2.0 nm. Annealing these films at 200 ^{o}C reduced R_{rms} to 1.7 nm without a significant change in morphology. Annealing at 300 ^{o}C resulted in oriented vertical growth of the grains accompanied by a significant increase in R_{rms} to 5.3 nm. The conversion into vertical growth may be attributed to the increase in thickness. A similar behavior was observed in aluminum-doped zinc oxide thin films [58]. Further annealing up to 500 ^{o}C did not change the morphology, although R_{rms} progressively increased to 7.2 nm. The roughness behavior against annealing temperature of these films is shown in figure 3.7.

Figure 3.8 shows the variation of lateral mean grain size with annealing temperature. The lateral mean grain size was increased monotonically with annealing and the increase in lateral grain size was due to the fusion of adjacent grains when sufficient energy is provided by the annealing process [59].

The morphology of reactively evaporated films on unheated substrate (RO films) is shown by the three dimensional AFM images in figure 3.9. The as-deposited films had a columnar microstructure but transformed into granular structure while annealing at 200 ^{o}C and 300 ^{o}C. The films showed a smooth surface structure at 400 ^{o}C which may be due to the coalescence of grain boundaries of granular structure. However, the surface turned back into columnar structure when the films were annealed at 500 ^{o}C. The films

deposited on heated substrate in oxygen (HO films) showed columnar structure throughout the annealing process as shown by the AFM three dimensional images in figure 3.10**.** The columnar microstructure of RO and HO films at 500 ^{o}C may be explained on the basis of the Thornton structure zone model [60], which predicts such a structure for $0.3 < T/T_m < 0.5$, where T_m is the melting point of the material. In our case, T = 773 K and T_m = 1840 K. The validity of this model is supported by the XRD results, which indicated that these films consisted of a single phase material (α-Fe_2O_3).

The variations in lateral mean grain size with annealing of these films is shown in figure 3.8. RO and HO films had larger lateral mean grain size at annealing temperature 300 ^{o}C and 400 ^{o}C, but decreased at 500 ^{o}C. The surface roughness R_{rms} = 2.8 ± 0.3 nm of RO films, and R_{rms} = 2.5 ± 0.2 of HO films, did not change significantly with annealing temperatures**.** Figure 3.7 also shows the behavior of roughness of these films with annealing.

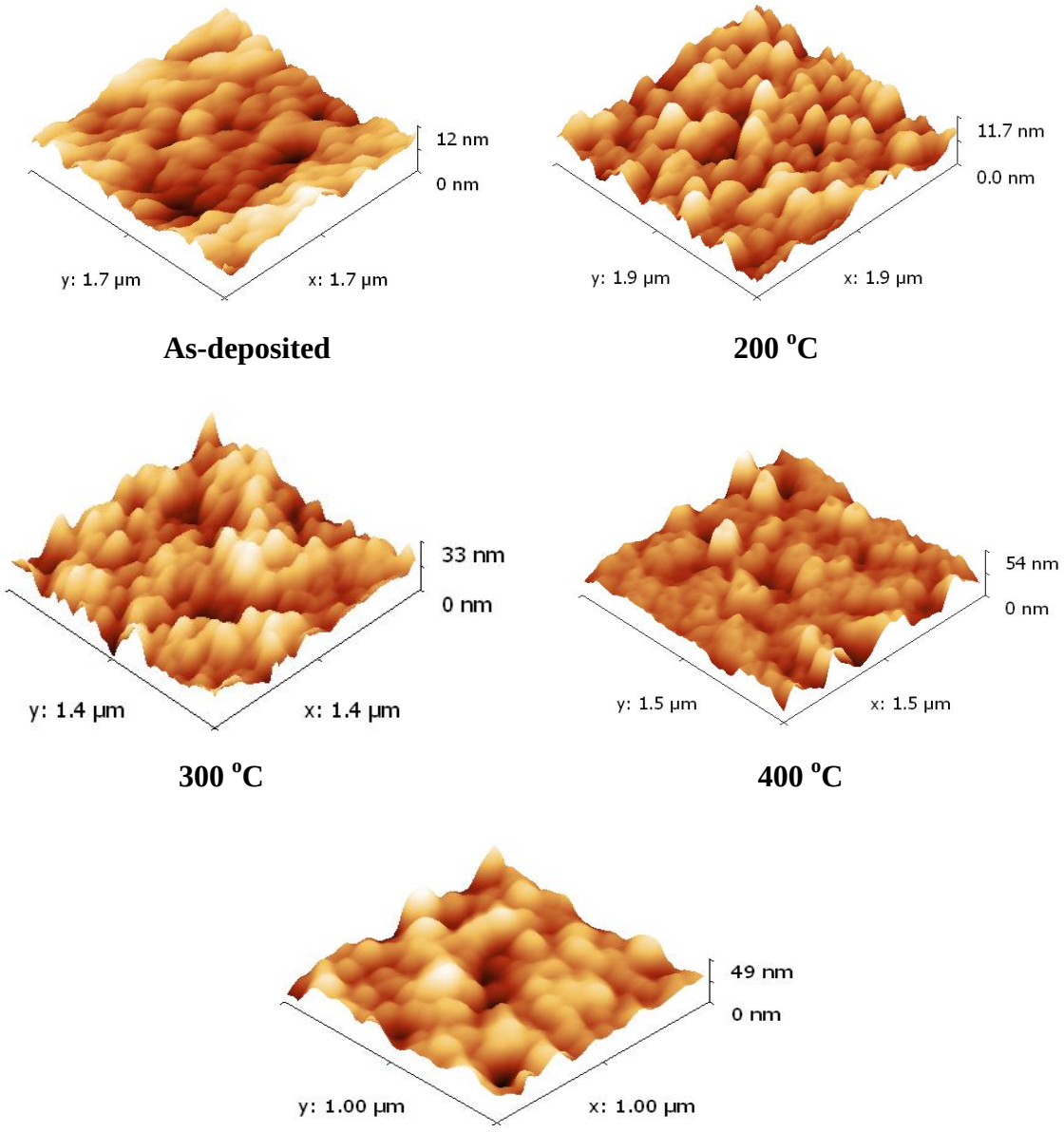

Figure 3.6. Three dimensional AFM images of the films deposited on unheated substrates in vacuum (RW films), and annealed at indicated temperatures.

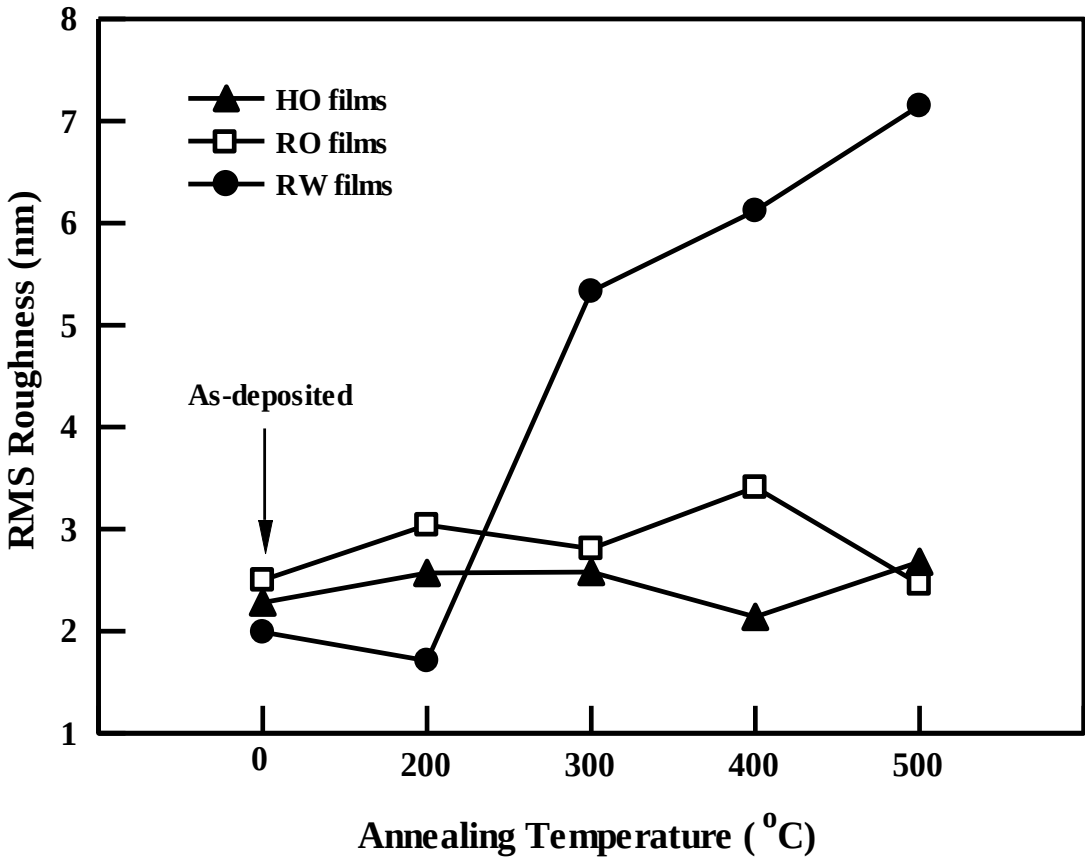

Figure 3.7. Surface roughness of the films obtained from AFM as a function of annealing temperature.

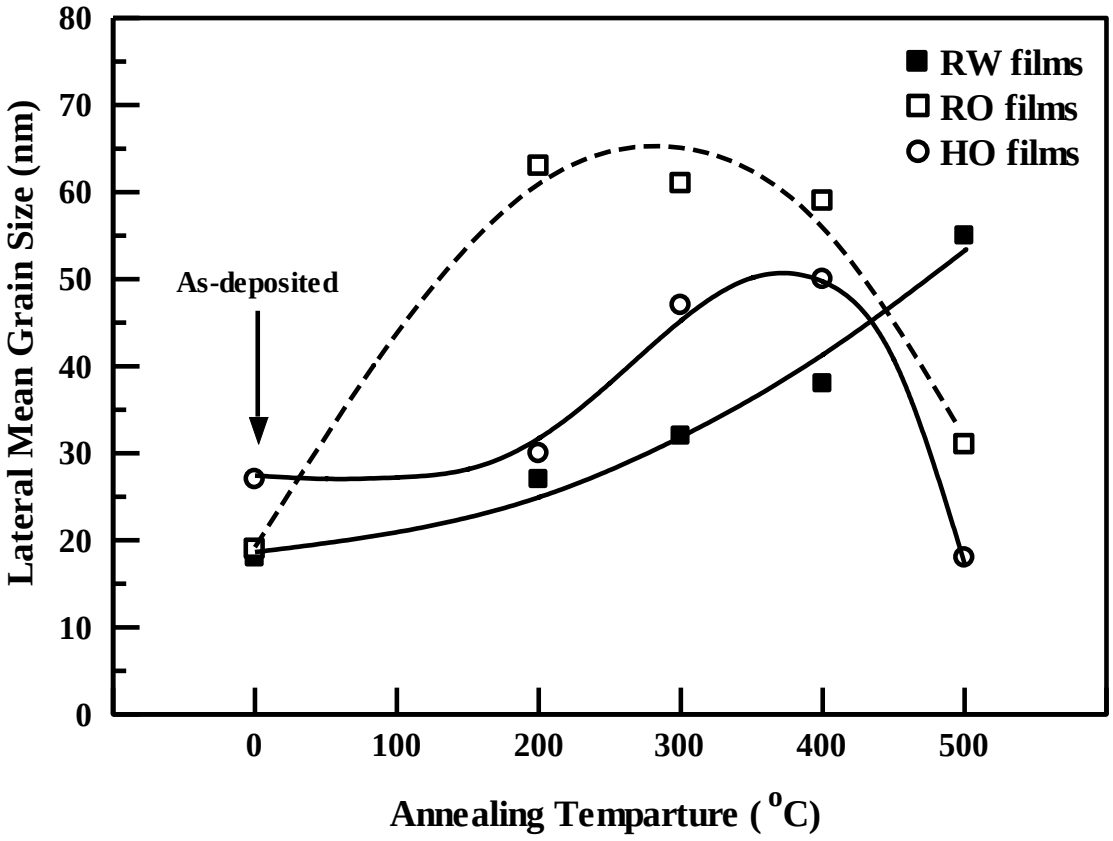

Figure 3.8. Lateral mean grain size of the films obtained from AFM as a function of annealing temperature.

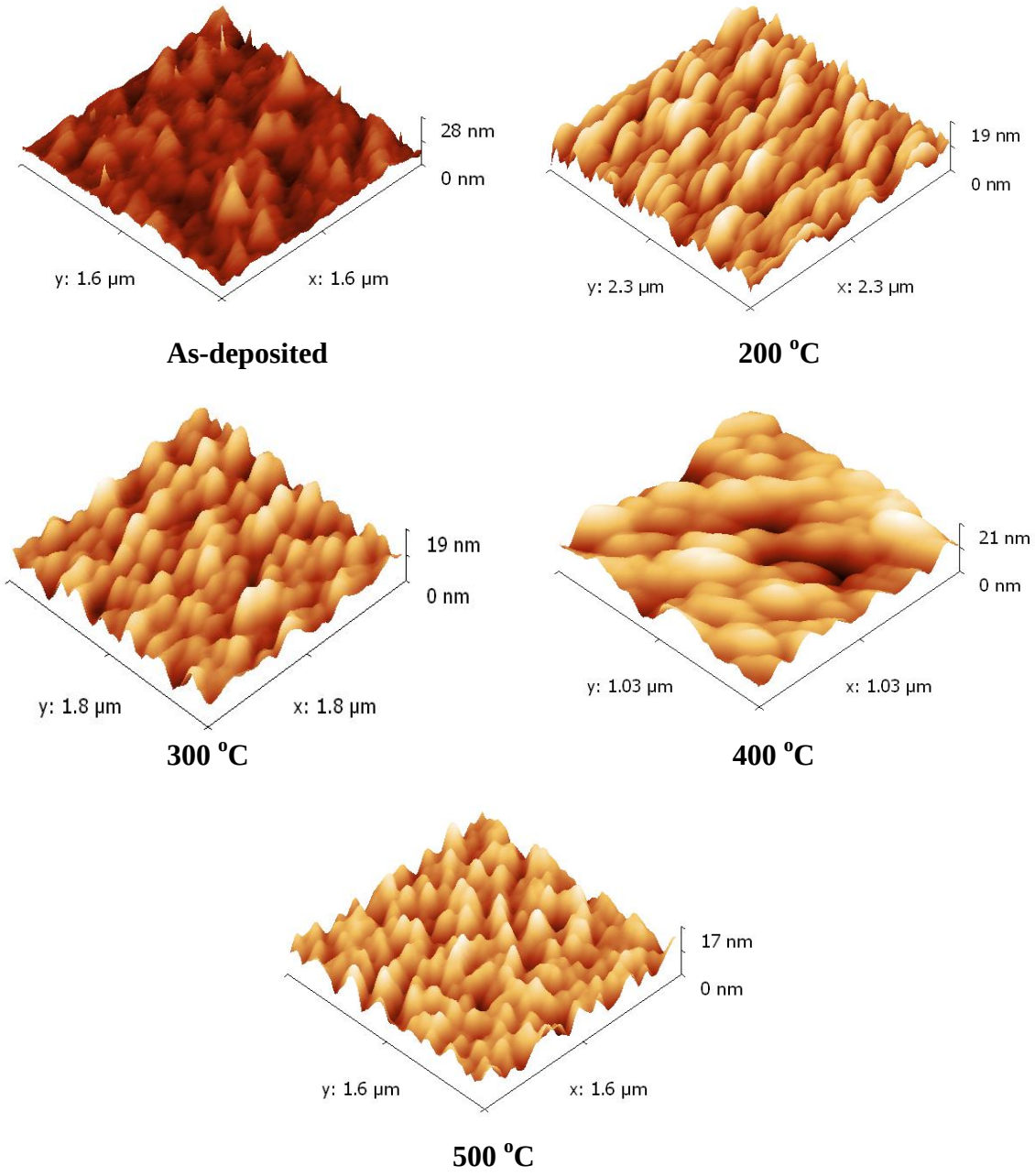

Figure 3.9. Three dimensional AFM images of the films deposited on unheated substrates in oxygen (RO films), and annealed at indicated temperatures.

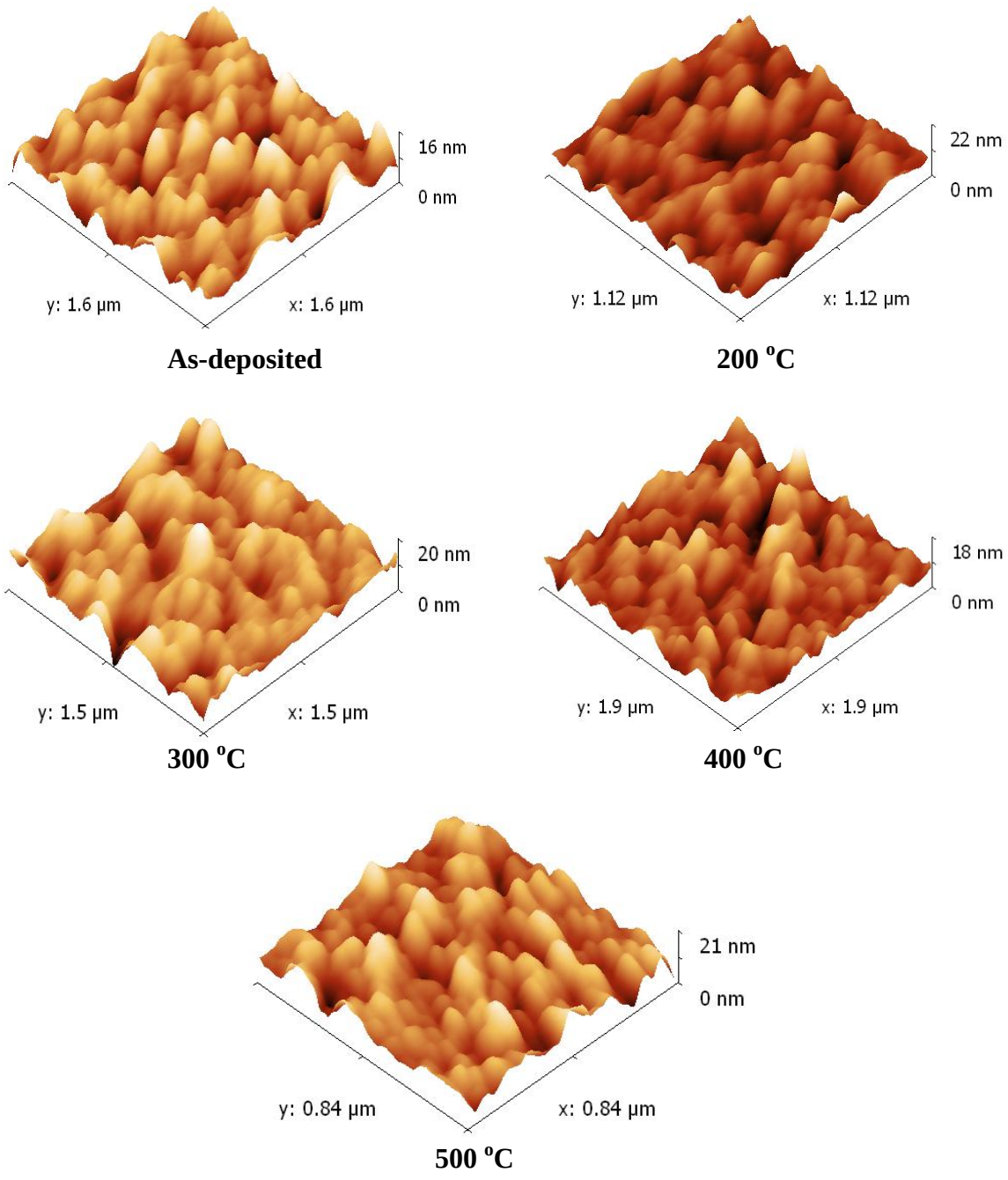

Figure 3.10. Three dimensional AFM images of the films deposited on heated substrates in oxygen (HO films), and annealed at indicated temperatures.

CHAPTER 4

Chemical Properties

The iron 2p level consists of two sublevels, $2p_{3/2}$ and $2p_{1/2}$ due to spin-orbit splitting. The $2p_{3/2}$ level consists of different binding energies which depend on the oxidation state of iron. The most common oxidation states of iron are metallic iron (Fe^0), ferrous oxide (Fe^{2+}), and ferric oxide (Fe^{3+}). The binding energy of Fe $2p_{3/2}$ in metallic iron (Fe^0), is in the range 706.7 – 707.4 eV [45,61–63]. The reported values for the binding energy of Fe $2p_{3/2}$ in the Fe^{2+} state are in the range 709.3 – 710.0 eV [45,61–66]. The reported values for the binding energy of Fe $2p_{3/2}$ in the Fe^{3+} state are in the range 710.6 – 711.6 eV [45,61–67]. The shake-up satellite peaks at the high binding energy side of $2p_{3/2}$ are considered to be characteristic of the Fe^{2+} and Fe^{3+} states. Theses satellites exist at different binding energies for different oxidation states. Therefore, these are frequently used in order to identify the iron oxide phases. The satellite peaks for FeO have been found at binding energies in the range 715 – 716 eV [45,61], and for Fe_2O_3 at binding energies in the range 719.0 – 719.8 eV [45,61,64,66]. Magnetite (Fe_3O_4) contains ⅓ Fe^{2+} ions and ⅔ Fe^{3+} ions [66], and has no satellite structure [61]. Detailed values for the binding energies in the Fe $2p_{3/2}$ region can be found in Ref. [61].

The O 1s spectrum in iron oxides consists of two components. The first component which is at the low binding energy (LBE) side corresponds to the Fe–O bond. The range of binding energies of the LBE component is 529.8 – 530.6 eV, and is independent of the oxidation state of iron [45,61,62,66,67]. The second component in the O 1s spectrum is at the high binding energy (HBE) side which corresponds to a binding energy ≥ 532 eV. This component is attributed to chemisorbed oxygen or absorbed moisture [45,62].

There have been some difficulties in interpreting XPS data related to iron oxides. These difficulties have been attributed to several factors. First, the correlation effects among the Fe 3d and O 2p states give rise to complicated multiplet structures [67]. Second, it is very difficult to prepare clean surfaces with controlled stoichiometry, and XPS spectra are easily influenced by the presence of contamination such as water and hydrocarbons at the surface [67]. Third, the binding energies were found to depend on the thickness of the oxide films. Variations of as much as 0.5 eV have been reported for films of different thicknesses [3]. In the case of oxidation, this is explained as follows. At first FeO is formed, then as the oxide thickness increases, Fe_2O_3 and Fe_3O_4 are formed on top of the FeO layer [62]. Finally, several levels were used as the binding energy reference, such as the gold Au $4f_{7/2}$ [61,68], the carbon C 1s although with different binding energies [62,69], the molybdenum Mo $3d_{5/2}$ [45], and the oxygen O 1s [44,67,70].

A typical XPS wide survey scan is shown in figure 4.1, and reveals that the only elements present were the constituent elements (Fe and O) and adventitious carbon. In addition to the wide survey scans, detailed high-resolution spectra were obtained in the Fe 2p and O 1s core level regions. The Fe 2p spectra for films deposited in vacuum on unheated substrates (RW films), films deposited on unheated substrates in oxygen (RO films) and

films deposited on heated substrates in oxygen ambient (HO films) are shown in figure 4.2, figure 4.3 and figure 4.4, respectively. The Fe $2p_{3/2}$ peak broadening for all films is due to the existence of multiple oxidation states of iron. Also, the Fe $2p_{3/2}$ spectrum had a highly asymmetric lineshape due to the presence of several oxidation states and satellites. In order to investigate the presence of different oxidation states of iron, the Fe $2p_{3/2}$ spectrum was resolved into constituent components using a Gaussian/Lorenzian mixed function employing Shirley background correction, as shown in figure 4.5. The weight (W) of a component was found by dividing the area under that component by the total area under the Fe $2p_{3/2}$ peak. Initially, we attempted to resolve the Fe $2p_{3/2}$ into three components (Fe^0, Fe^{2+}, Fe^{3+}). However, the metallic component (Fe^0) was only found in as-deposited RW films (figure 4.2), with a very small weight of 0.02. Thus, the Fe $2p_{3/2}$ peak was resolved into two components (Fe^{2+} and Fe^{3+}). These components were not well separated due to strong multiplet splitting [45]. The binding energies (BE), weight (W), and the full width at half maximum (Γ) of the two components are listed in table 4.1. The spin orbit splitting (δ_{2p}) between the Fe $2p_{3/2}$ and the Fe $2p_{1/2}$ peaks is also given in table 4.1. Its value was very close to that reported in the literature [62,69]. The XPS results indicate that the surfaces of the iron films were oxidized as soon as they were exposed to air. Exposure of iron to oxygen, even at room temperature, results in the adsorption of oxygen and the formation of a few monolayers of $Fe^{2+}$and Fe^{3+}oxides [45,62]. As-deposited RW films were not showing apparent satellite features and had $2p_{3/2}$ peak at a binding energy of 710.9 eV. This indicated the formation of Fe_3O_4 as the films were exposed to the air/moisture environment. However in all other films, the satellite peaks were observed. The satellites were observed at binding energies of $18.5 - 19.7$ eV,

characteristic of Fe_2O_3. There were no satellites observed at binding energies of 715 – 716 eV, indicating no signature of FeO. The lack of the satellites characteristic of films reveal the presence of Fe_3O_4 on the surfaces of the films. Although the XRD results showed that the annealing of iron resulted in the formation of Fe_2O_3, the XPS results indicated that the surface of the films contained both Fe_3O_4 and Fe_2O_3 species, albeit with a predominant Fe_2O_3 component.

The O 1s spectra were resolved into two components as shown in figure 4.6. The first component (LBE) corresponds to oxygen bound to iron. The second component (HBE) corresponds to chemisorbed oxygen. The binding energy (BE), weight (*W*), and full width at half maximum (*Γ*) of each component are given in Table 4.1. On average, the HBE component was 12% of the total O 1s peak for films deposited on unheated substrates (RW and RO films). Its value was significantly reduces to 6% for film deposited on heated substrates (HO films). The intensity of this component is partly proportional to the amount of adsorbed water, which in turn is expected to increase with the porosity of the films. This is consistent with the compact nature of HO films, as revealed by their lower thickness.

Iron oxide (Fe_2O_3) thin films were also analyzed quantitatively. Table 4.2 showed the obtained values of oxygen to iron ratio [O/Fe]. For Fe_2O_3, the [O/Fe] is 1.5, however the values obtained (as shown in table) are higher than 1.5. We noticed that this discrepancy is due to two reasons. Firstly, unfriendly behavior of software during the analysis, secondly, the asymmetric and broad nature of O 1s peaks obtained from XPS analysis. The excess of high binding energy oxygen (moisture) and lack of information, like peak width and peak height etc. of low binding energy oxygen (lattice oxygen). In order to

obtain the desire [O/Fe], a pure Fe_2O_3 as reference is required to analyze. Then the information of multiple components peaks of O 1s of pure Fe_2O_3 can be use as reference for all thin films to get the acceptable [O/Fe].

Table 4.1. Summary of the XPS results of the films.

Type	T_a (°C)	Fe $2p_{3/2}$								O 1s						Δ (eV)
		Fe^{2+}			Fe^{3+}					LBE			HBE			
		BE (eV)	Γ (eV)	*W*	*BE* (eV)	Γ (eV)	*W*	Sat. (eV)	δ_{2p} (eV)	*BE* (eV)	Γ (eV)	*W*	*BE* (eV)	Γ (eV)	*W*	
RW	As	709.8	3.1	0.46	711.3	3.7	0.52	---	13.8	530.0	2.1	0.87	532.0	1.6	0.13	180.9
	200	709.9	1.7	0.18	711.2	3.7	0.82	718.6	13.5	529.9	1.9	0.87	532.0	1.8	0.13	181.0
	300	709.7	1.8	0.25	711.4	3.5	0.75	718.6	13.3	529.7	1.9	0.86	532.0	2.0	0.14	181.1
	400	709.9	1.6	0.16	711.6	3.6	0.84	718.6	13.6	529.8	1.7	0.89	531.9	1.9	0.11	181.3
	500	710.0	1.6	0.11	711.3	3.6	0.89	718.9	13.3	530.0	1.9	0.92	531.7	2.0	0.08	181.2
RO	As	709.8	1.8	0.19	711.2	3.5	0.81	719.0	13.6	530.0	2.1	0.88	532.6	2.0	0.12	181.1
	200	710.0	1.7	0.18	711.3	3.9	0.82	718.6	13.7	530.0	2.3	0.91	532.6	1.9	0.11	181.0
	300	709.9	1.7	0.19	711.3	3.6	0.81	719.3	13.2	529.8	2.0	0.86	532.0	2.0	0.14	181.1
	400	709.9	1.7	0.16	711.0	3.7	0.84	719.7	13.7	529.8	2.1	0.90	532.4	2.2	0.10	181.1
	500	709.9	1.7	0.19	711.4	3.9	0.81	719.5	13.8	529.7	1.9	0.90	532.0	2.0	0.10	181.2
HO	As	709.7	1.8	0.20	711.3	3.7	0.80	719.3	13.2	529.8	1.9	0.94	532.3	1.9	0.06	181.1
	200	709.7	1.8	0.24	711.3	3.9	0.76	718.5	13.7	529.6	2.2	0.94	532.2	2.0	0.06	181.2
	300	709.9	1.7	0.20	711.2	3.9	0.80	718.8	13.3	530.0	2.0	0.92	532.5	2.1	0.08	180.7
	400	709.8	1.6	0.17	711.4	3.6	0.83	719.1	13.9	529.9	2.0	0.98	532.4	1.8	0.02	181.1
	500	709.7	1.8	0.24	711.3	3.5	0.76	718.6	13.6	529.7	1.7	0.98	532.3	2.4	0.02	181.1

*δ_{2p} is the BE difference between the Fe$2p_{3/2}$ and Fe $2p_{1/2}$ peaks, Δ is the *BE* separation between the Fe $2p_{3/2}$ and O 1s peaks, *W* is the weight of the component, Γ is the full width at half maximum, Sat. is the satellite peak.

Table 4.2. Summary of quantitative results of the films.

Films	Annealing temperature (^{o}C)	Fe 2p3/2		O 1s		[O/Fe]
		[AT]%	SF	[AT]%	SF	
RW	As	33.5	10.82	66.5	2.93	2.0
	200	21.2	10.82	78.8	2.93	3.7
	300	25.8	10.82	74.2	2.93	2.9
	400	33.7	10.82	66.3	2.93	2.0
	500	13.8	10.82	86.2	2.93	6.2
RO	As	21.1	10.82	78.9	2.93	3.7
	200	19.8	10.82	80.2	2.93	4.0
	300	21.7	10.82	78.3	2.93	3.6
	400	25.5	10.82	74.5	2.93	2.9
	500	20.5	10.82	79.5	2.93	3.9
HO	As	23.7	10.82	76.3	2.93	3.2
	200	24.1	10.82	75.9	2.93	3.1
	300	23.4	10.82	76.6	2.93	3.3
	400	25.7	10.82	74.3	2.93	2.9
	500	24.2	10.82	75.8	2.93	3.1

*****SF is the sensitivity factor

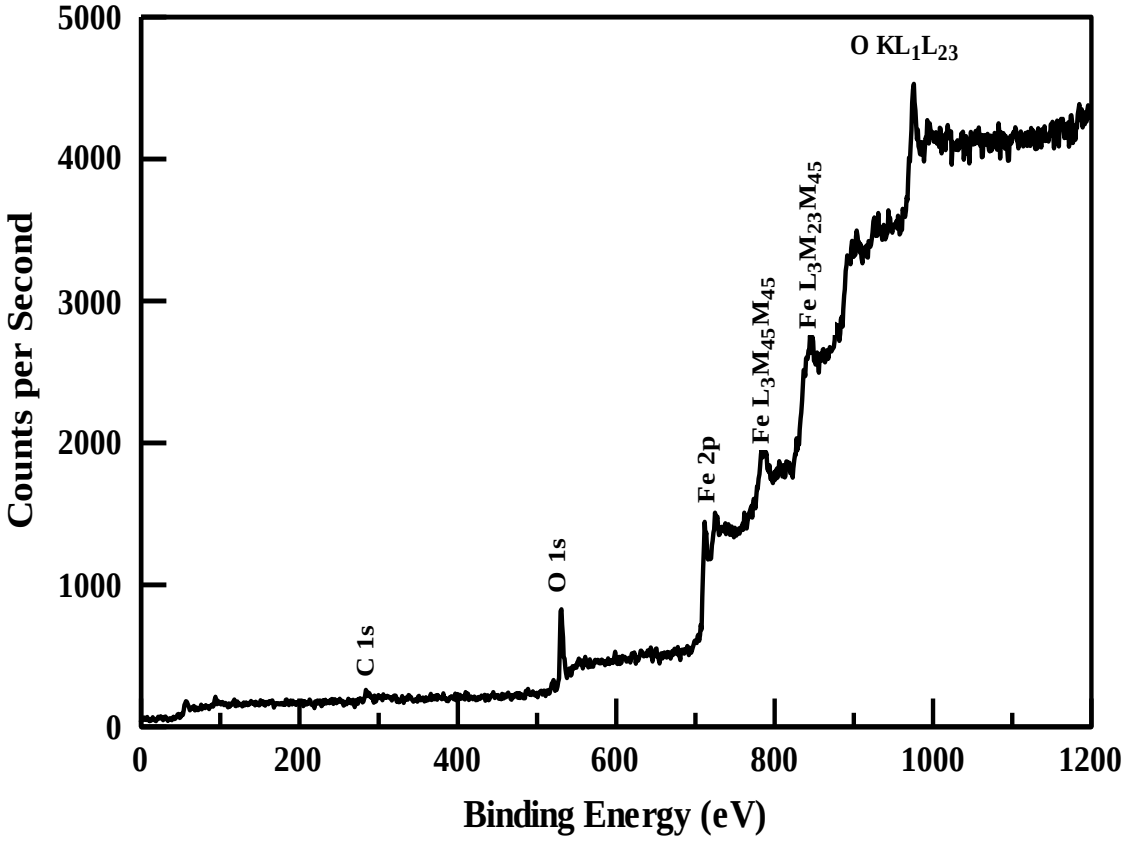

Figure 4.1. A typical XPS wide survey scan of the films.

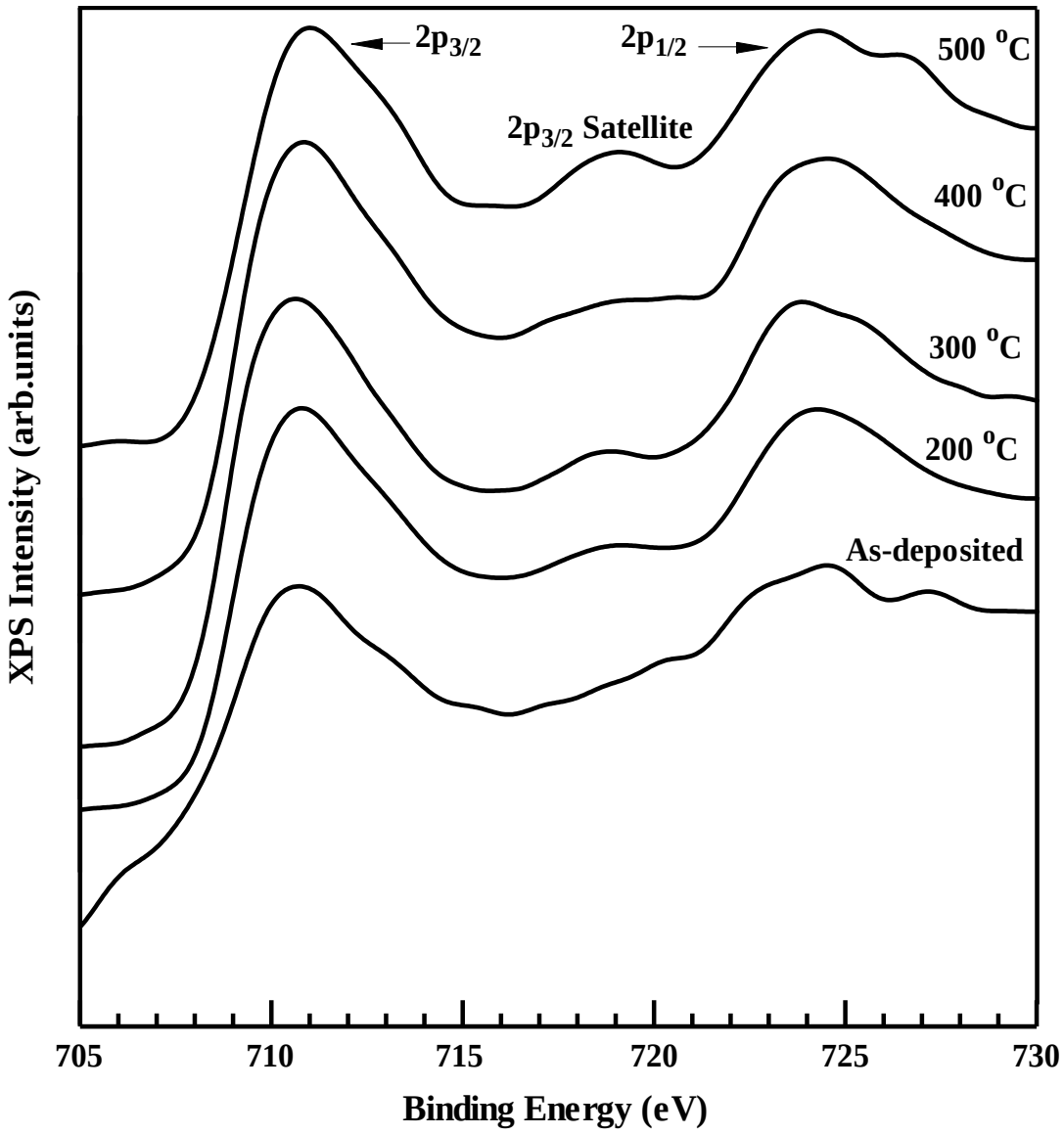

Figure 4.2. Fe 2p spectra of the films deposited on unheated substrates in vacuum (RW films), and post annealed at 200 − 500 °C.

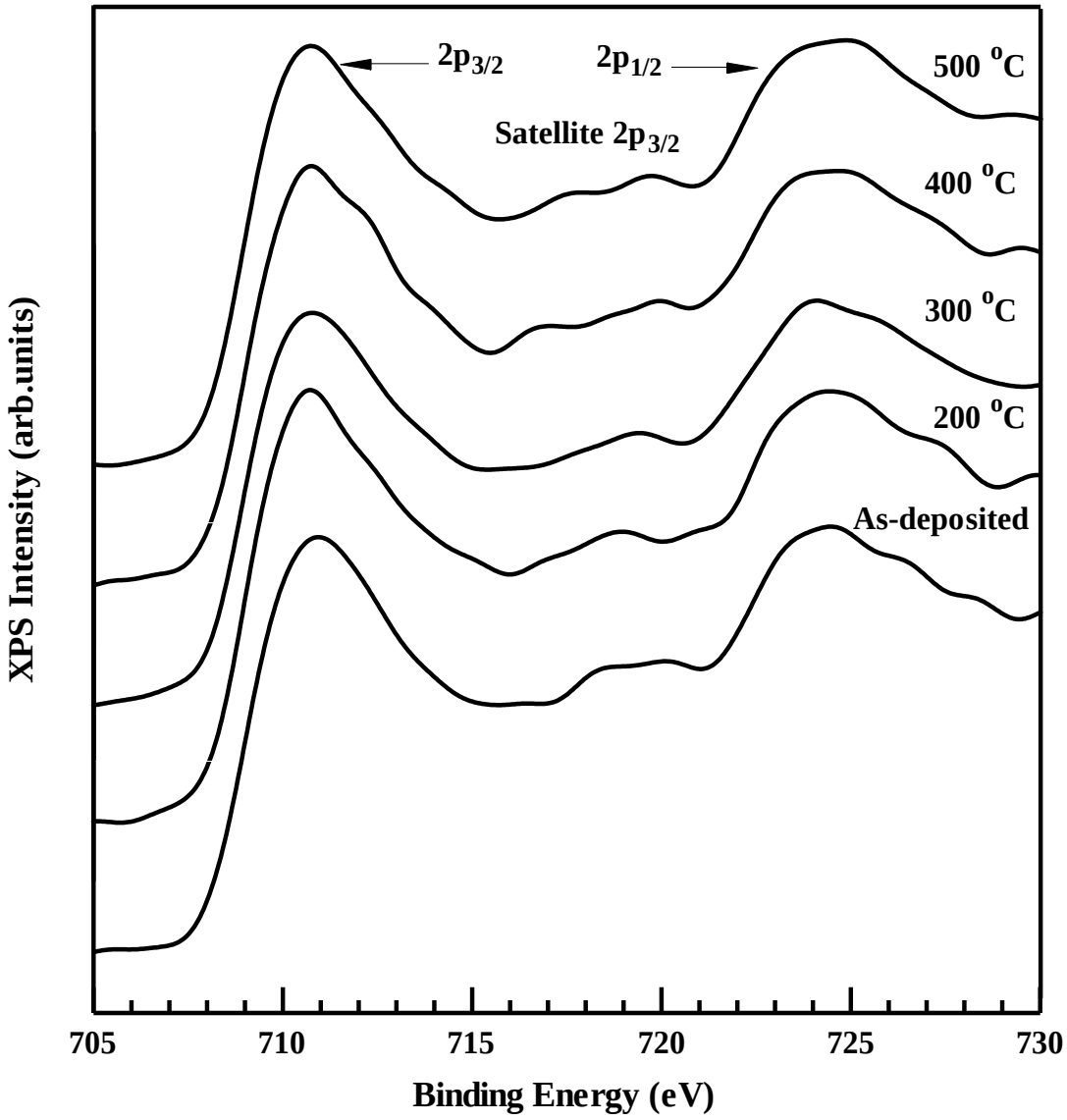

Figure 4.3. Fe 2p spectra of the films deposited on unheated substrate in oxygen (RO films), and post annealed at 200 − 500 °C.

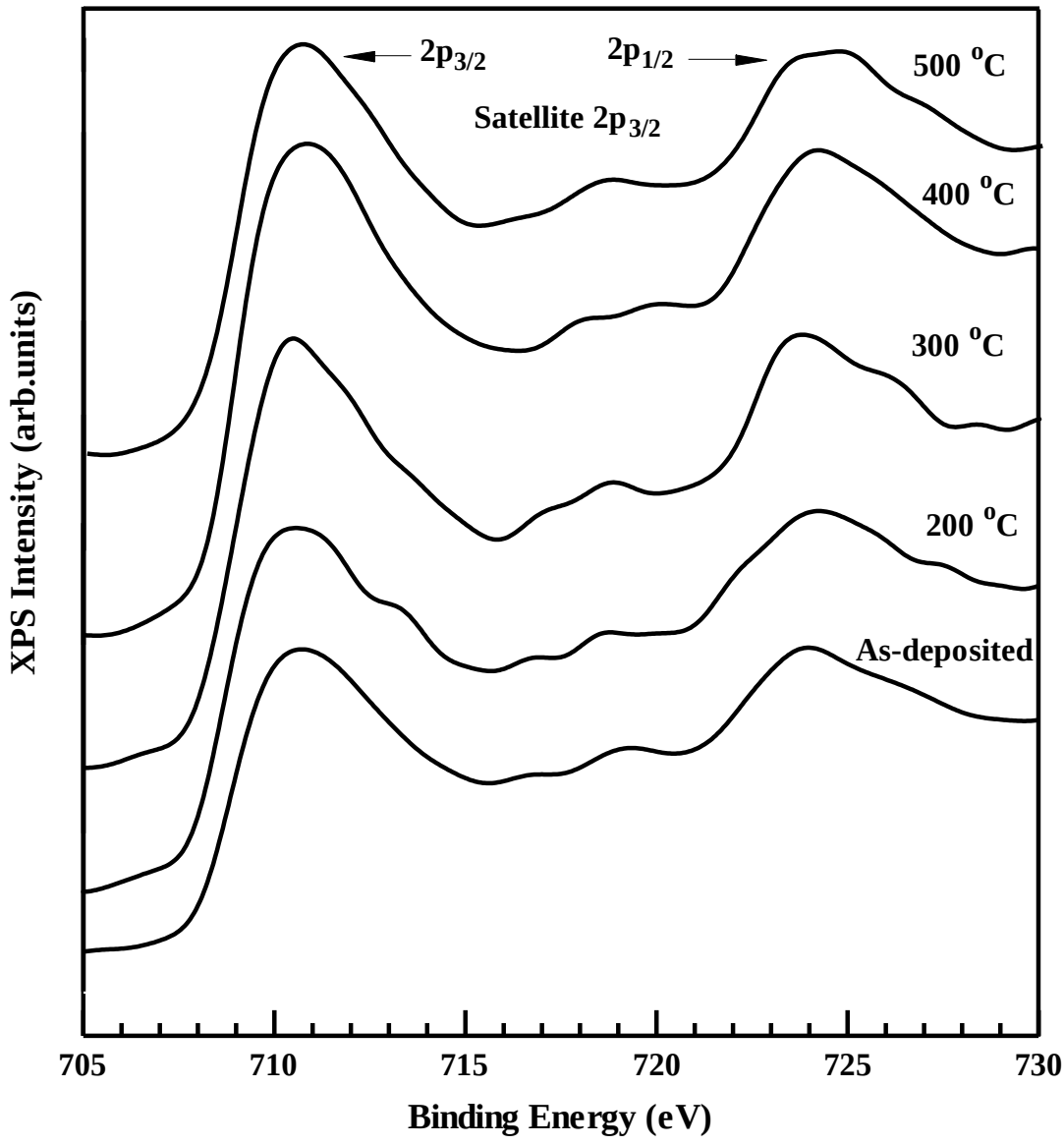

Figure 4.4. Fe 2p spectra of the films deposited on heated substrate in oxygen (HO films), and post annealed at 200 − 500 °C.

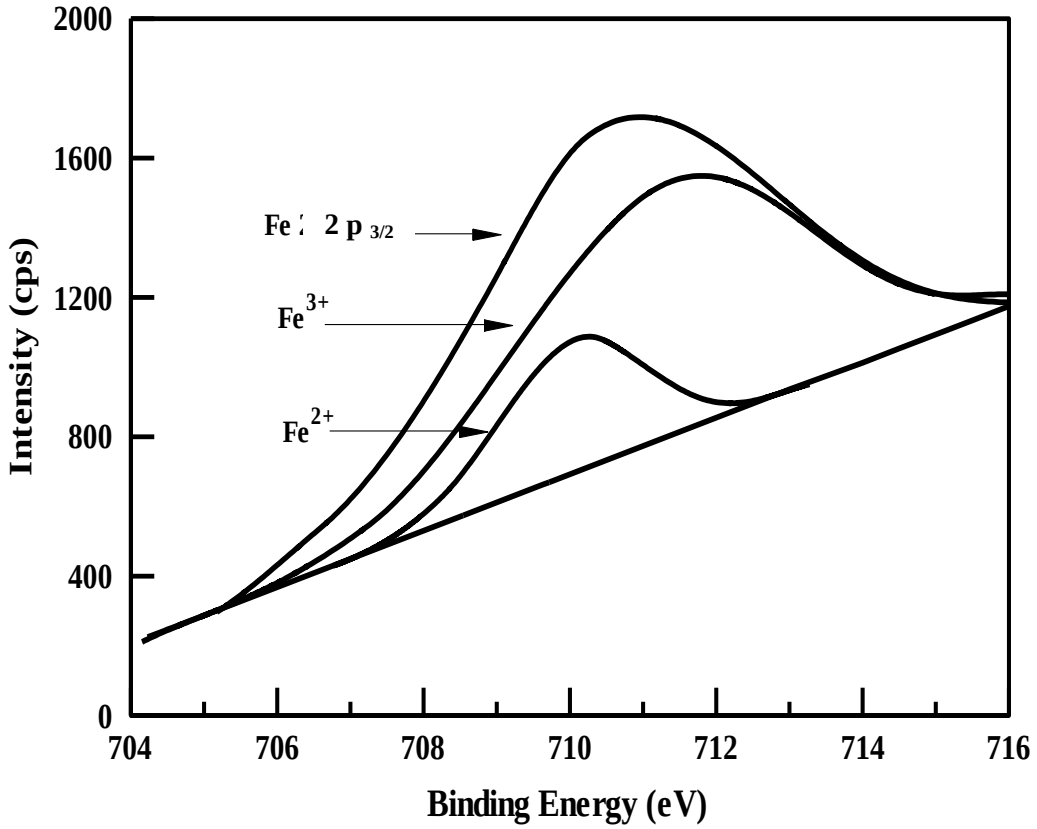

Figure 4.5. Resolution of the Fe $2p_{3/2}$ peak into two components corresponding to the two oxidation states of iron.

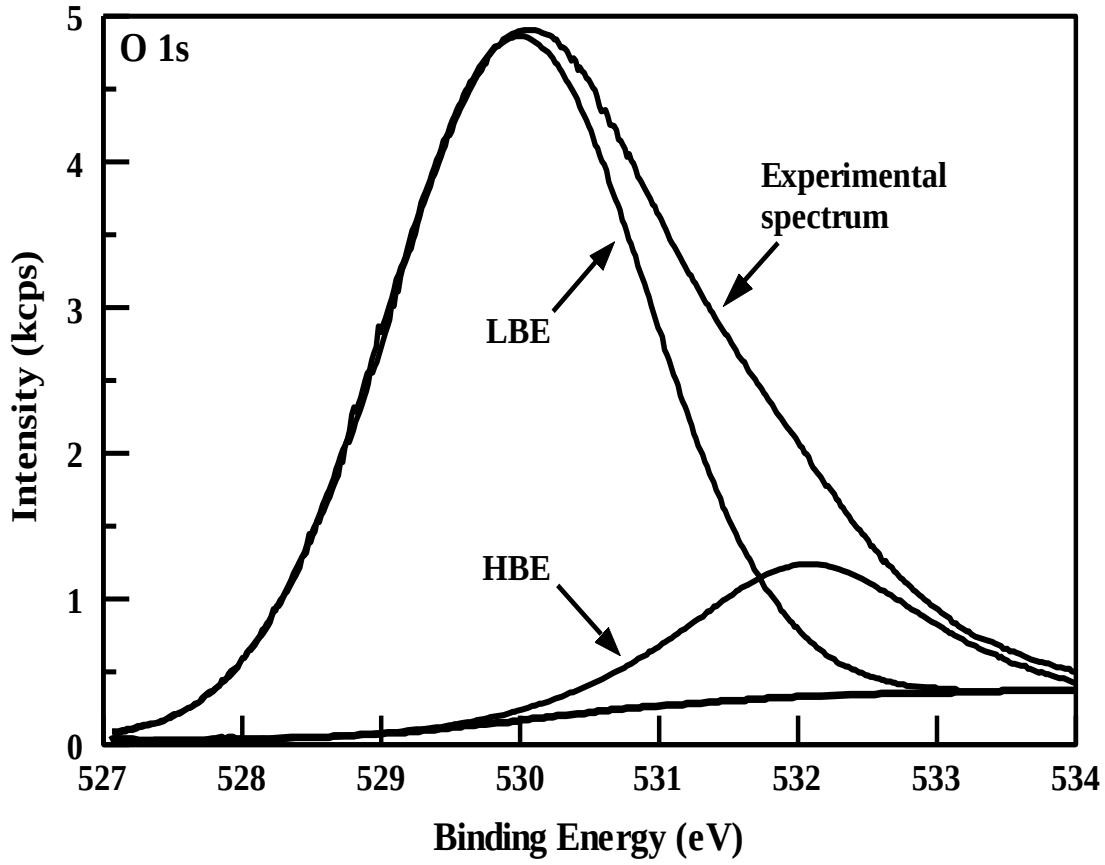

Figure 4.6. Resolution of the XPS O 1s spectrum into low binding energy (LBE) component corresponding to the Fe – O bond, and high binding energy (HBE) component corresponding to chemisorbed oxygen.

CHAPTER 5

Optical Properties

Optical applications necessitate knowledge about the optical properties of the material. These include the refractive index (n), extinction coefficient (k), absorption coefficient (α), and the band gap (E_g). The optical properties of thin films are sensitively dependent on the preparation conditions and the models used to extract the optical constants from measured quantities. It is desirable to determine these properties as functions of the wavelength of light (or photon energy). In the case of the refractive index, such a relation constitutes the dispersion properties of the material.

5.1 OPTICAL CONSTANTS

Figures 5.1 and 5.2 show, respectively, the transmittance and reflectance of the films deposited on unheated substrates in vacuum (RW films). The transmittance spectra (figure 5.1) show that the as-deposited films and those annealed at 200 ^{o}C and 300 ^{o}C were opaque with poor transmittance. However, the transmittance of the films was improved upon annealing at 400 ^{o}C and 500 ^{o}C. The RW films consisted of elemental iron and iron oxide at annealing temperature 200 ^{o}C and 300 ^{o}C, and were transformed

into pure α-Fe_2O_3 phase at 400 ^oC and 500 ^oC as was shown by the XRD results in Chapter 3. These oxide films had polycrystalline structure with larger grain size and had high surface roughness. Because of high transparency of the oxide films, only the optical constants of RW films annealed at 400 ^oC and 500 ^oC were taken into account.

The transmittance and reflectance spectra of the films deposited on unheated substrate in oxygen (RO films) are shown in figures 5.3 and 5.4 respectively. Figures 5.5 and 5.6 respectively, show the transmittance and reflectance spectra the films deposited on heated substrates in oxygen (HO films). The surface morphology, oxygen vacancies, defects, and polycrystalline structure influence the optical properties of thin films. These factors can enhance the scattering of light and reduce the transmittance of the films. In transmittance and reflectance spectra, maxima and minima were due to multiple-beam interference in the transparent region of the films, which is a characteristic of dielectric films. The transmittance of RW films annealed at 400 ^oC was higher than the films annealed at 500 ^oC. The higher transmittance at 400 ^oC may be attributed to low surface roughness of the films. The R_{rms} values of the films annealed at 400 ^oC was 6.2 nm, and was increased to 7.2 nm when the films were annealed at 500 ^oC. However the transmittance spectra for RO and HO films did not change significantly with annealing, which is due to fact that the roughness of films was not changed considerably as these films were annealed from 200 ^oC to 500 ^oC. The transmittance of all films was decreasing for wavelength 700 nm to 200 nm which is due to the fundamental absorption of semiconductors in UV-Vis-region. It should be noted that in some of the spectra there is a small kink appearing in between $800-900$ nm which is due to the change of grating from IR region to Vis-region.

In the transparency region of the films ($\lambda \geq 600$ nm), the transmittance spectra can be used to determine the optical constants of the films. The transmittance of a transparent film on a transparent substrate is given by [71,72]

$$T = \frac{16n_s(n^2 + k^2)\beta}{A + B\beta^2 + 2\beta\left[Ccos\left(4\pi nd/\lambda\right) + Dsin\left(4\pi nd/\lambda\right)\right]} \quad (5.1)$$

where,

$A = [(n+1)^2 + k^2][(n + n_s) + k^2]$

$B = [(n-1)^2 + k^2][(n - n_s) + k^2]$

$C = -(n^2 - 1 + k^2)(n^2 - {n_s}^2 + k^2) + 4k^2 n_s$

$D = 2kn_s(n^2 - 1 + k^2) + 2k(n^2 - {n_s}^2 + k^2)$

and n_s is the refractive index of the substrate, d is the thickness of the film, λ is the wavelength of light, and $\beta = exp(-4\pi kd/\lambda)$.

In order to fit the experimental transmittance spectra using equation (5.1), the refractive index of the films was modeled by a single oscillator model [73]:

$$n = \left(1 + \frac{E_o\, E_d}{E_o^2 - E^2}\right)^2 \quad (5.2)$$

where E_o is the effective oscillator energy, E_d is the dispersion energy related to the inter band transition strength, and E is the incident photon energy ($E = hc/\lambda$). The dispersion energy (E_d) is directly related to the structural order of the films, where it increases with enhanced crystallinity [74]. The extinction coefficient of the films was modeled by Urbach law of exponential absorption below the band gap [75]:

$$k = k_o exp\left[\frac{E - E_1}{\delta}\right] \quad (5.3)$$

where k_o is a constant, E_1 is an energy representing the onset of sub-band gap absorption, and δ is the Urbach band energy width. The experimental transmittance spectra were fitted using equation (5.1), equation (5.2) and equation (5.3) as models for optical constant. The fitting parameters were E_o, E_d, E_1, k_o, and δ. The substrate refractive index was taken from reference [76]. The calculated transmittance spectra, employing the above models for *n* and *k* successfully fitted the experimental spectra throughout the transparency range with a correlation that was better than 99 %, as shown in figure 5.7.

The best-fit parameters are given in Table 5.1, and were used to calculate the optical constants of the films. Figures 5.8 and 5.9 show the dispersion curves for *n* and *k* of RW films, respectively. The values of *n* and *k* were increasing with decreasing wavelength, and attained their maximum values at wavelength of 600 nm. The refractive index of the films was also increased from 3.0 to 3.1 with annealing temperature. The increase in *n* with annealing may be attributed to the improvement of crystallinity of the films, as can be seen in figure 3.2. On the other hand, these films did not possess high values of *k*, which also increased with annealing temperature. The dispersion curves for *n* and *k* of RO films are shown in figure 5.10 and 5.11, respectively; while figures 5.12 and 5.13 show the dispersion curves for *n* and *k* of HO films, respectively. The refractive index of the films deposited on heated substrates (HO films) was higher than those of films deposited on unheated substrates (RO films). A similar trend was also observed in previous studies [77,78]. The variation of the refractive index with substrate temperature may be correlated with the density of the films. The low value of the refractive index for the RO films indicates that these films had relatively low packing density. Lowering of

the packing density is caused by the incorporation of oxygen during film growth [79], which may create voids that absorb moisture [80]. Moreover, collisions of the evaporated species with O_2 molecules reduce their kinetic energy before reaching the substrate, and this will result in lower packing density [80]. Substrate heating provides thermal energy that increases the mobility of the atoms of the films, thereby increasing the packing density of the films [81]. This is supported by three observations. First, the thickness of the HO films was less than that of RO films. Second, the RO films had columnar structure indicating that there were more voids in these films. Third, the dispersion energy (E_d) was larger for the HO films, which is also correlated with densification of the films [82]. An estimate of film density may be obtained from the Lorentz-Lorenz relation [83]:

$$\frac{\rho_f}{\rho_b} = \frac{(n_f^2 - 1)(n_b^2 + 2)}{(n_f^2 + 2)(n_b^2 - 1)} \qquad (5.4)$$

where ρ_f is the density of the film, ρ_b is the density of the bulk material, n_f is the film's refractive index, and n_b is the bulk refractive index, whose value for Fe_2O_3 is 2.918 at λ = 633 nm [84]. Using n_f values of 2.075 for RO films and 2.773 for HO films at λ = 633 nm, the relative density (ρ_f / ρ_b) was 0.73 for the RO films, and 0.97 for the HO films. This indicates the compact and dense nature of the HO films as compared to RO films. The extinction coefficient of HO films was also higher than RO films. Similar to the refractive index, the extinction coefficient increases for the higher-density films [85]. Dense packing will reduce the voids within the film and increase absorption. Moreover, the extinction coefficient of the HO films had non-zero values up to λ = 1200 nm. This is also supported by the larger Urbach band energy width (δ) of these films. The values of the refractive index reported in the literature showed great variation based on the

experimental technique and conditions, post-deposition treatment, and analytical techniques used to derive the refractive index. Therefore, it is not unusual to obtain different values of *n* and *k* from the reported values in literature [77,78,82].

Table 5.1. Summary of the best-fit parameters used in fitting the experimental transmittance spectra of the films

Type	Annealing Temperature ^{o}C	E_o (eV)	E_d (eV)	E_1 (eV)	k_o	δ (eV)
RW films	400	2.96	12.47	2.87	0.06	1.65
	500	2.88	12.45	3.85	0.11	2.55
RO films	As-deposited	2.94	5.42	2.23	0.17	0.12
	200	2.89	5.23	2.21	0.16	0.12
	300	2.81	4.74	2.21	0.18	0.13
	400	2.79	4.73	2.18	0.15	0.12
	500	2.65	4.01	2.20	0.19	0.13
HO films	As-deposited	3.16	13.04	2.27	0.02	0.75
	200	3.23	13.62	2.50	0.08	0.42
	300	3.17	13.10	2.60	0.07	0.51
	400	3.29	14.04	2.56	0.20	0.34
	500	3.10	12.67	2.74	0.11	0.49

RW: films deposited on unheated substrates in vacuum, RO: films deposited on unheated substrates in oxygen, HO: films deposited on heated substrates in oxygen

.

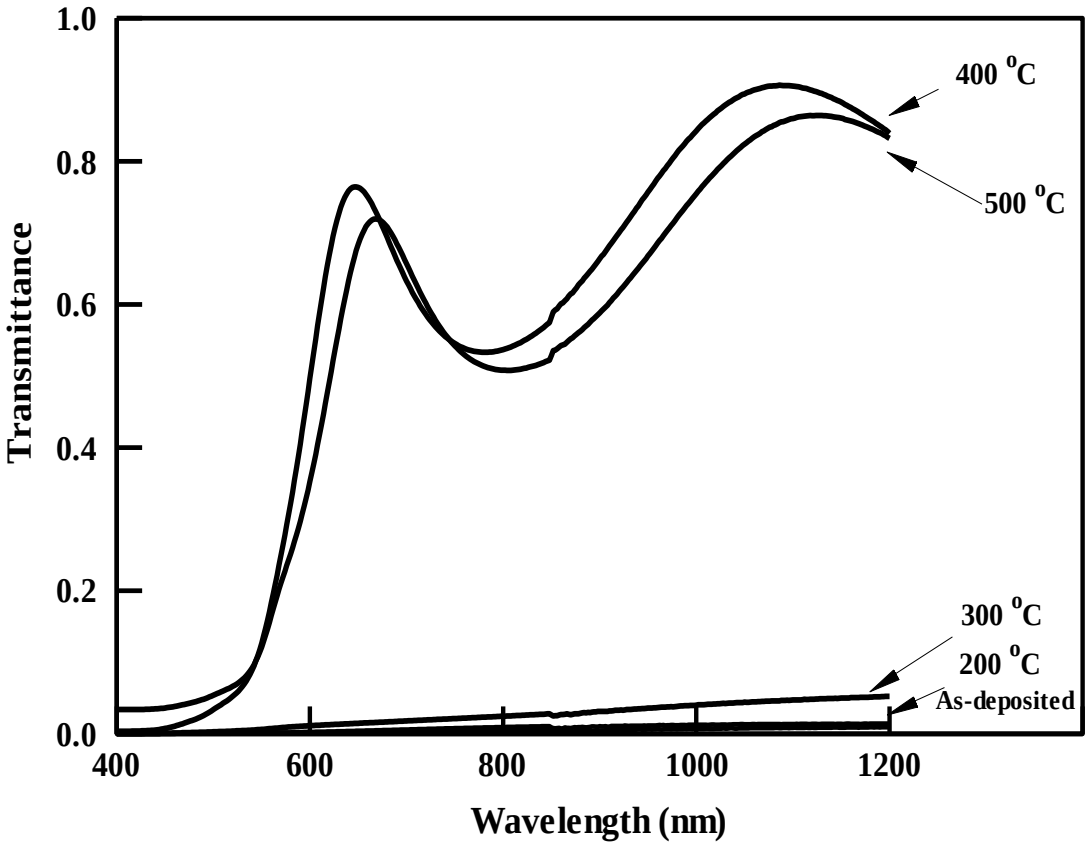

Figure 5.1. Measured normal-incidence transmittance spectra of the films deposited on unheated substrates in vacuum (RW films).

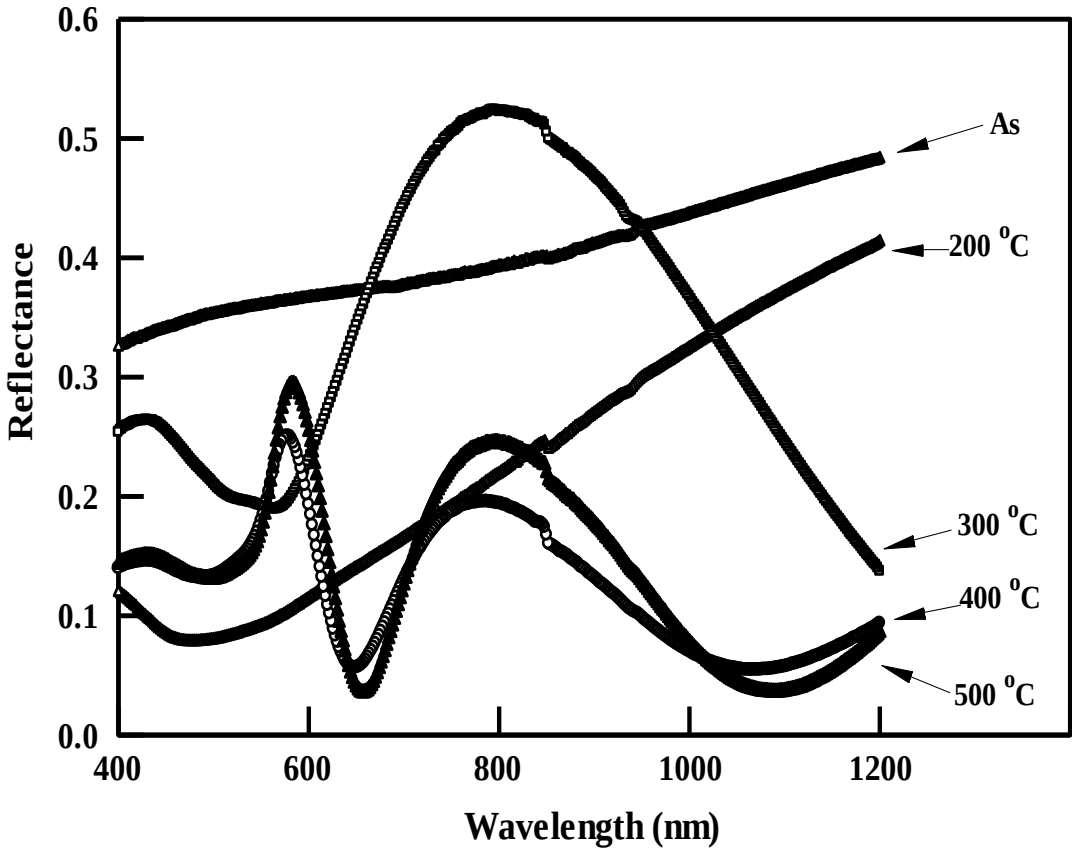

Figure 5.2. Measured normal-incidence reflectance spectra of the films deposited on unheated substrates in vacuum (RW films).

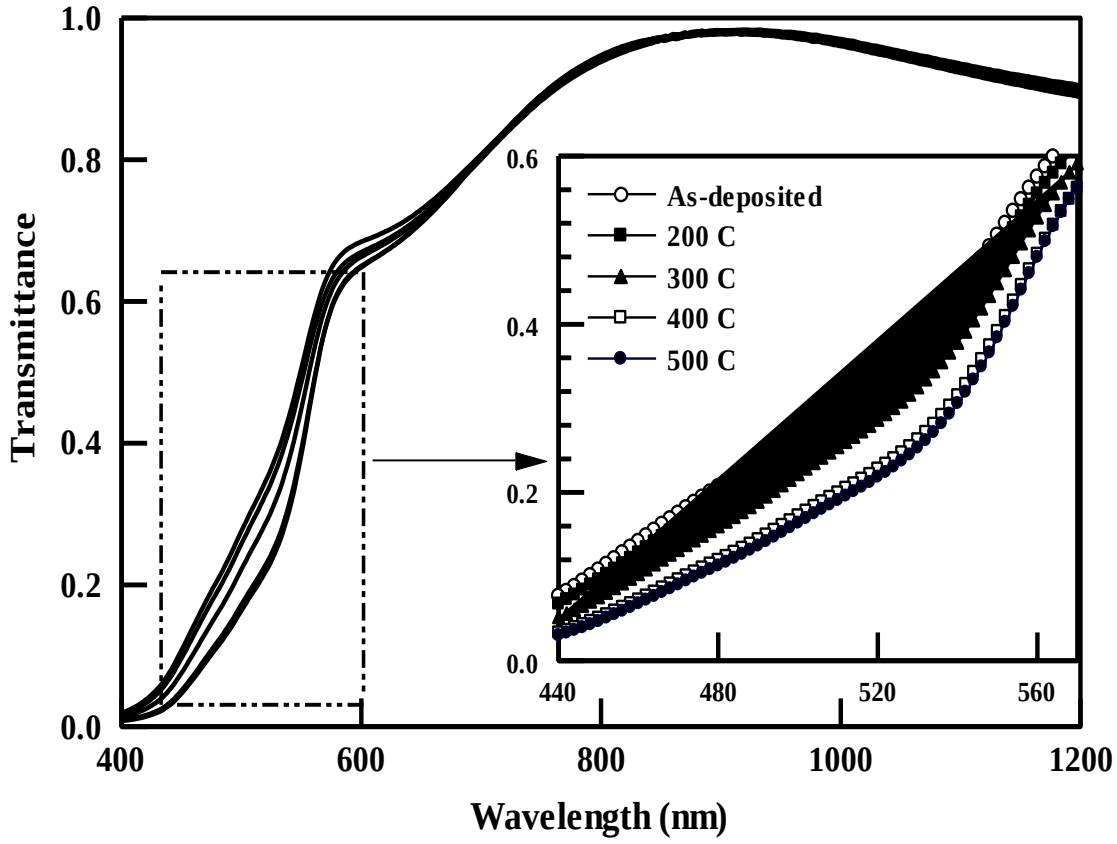

Figure 5.3. Measured normal-incidence transmittance spectra of the films deposited on unheated substrates in oxygen (RO films).

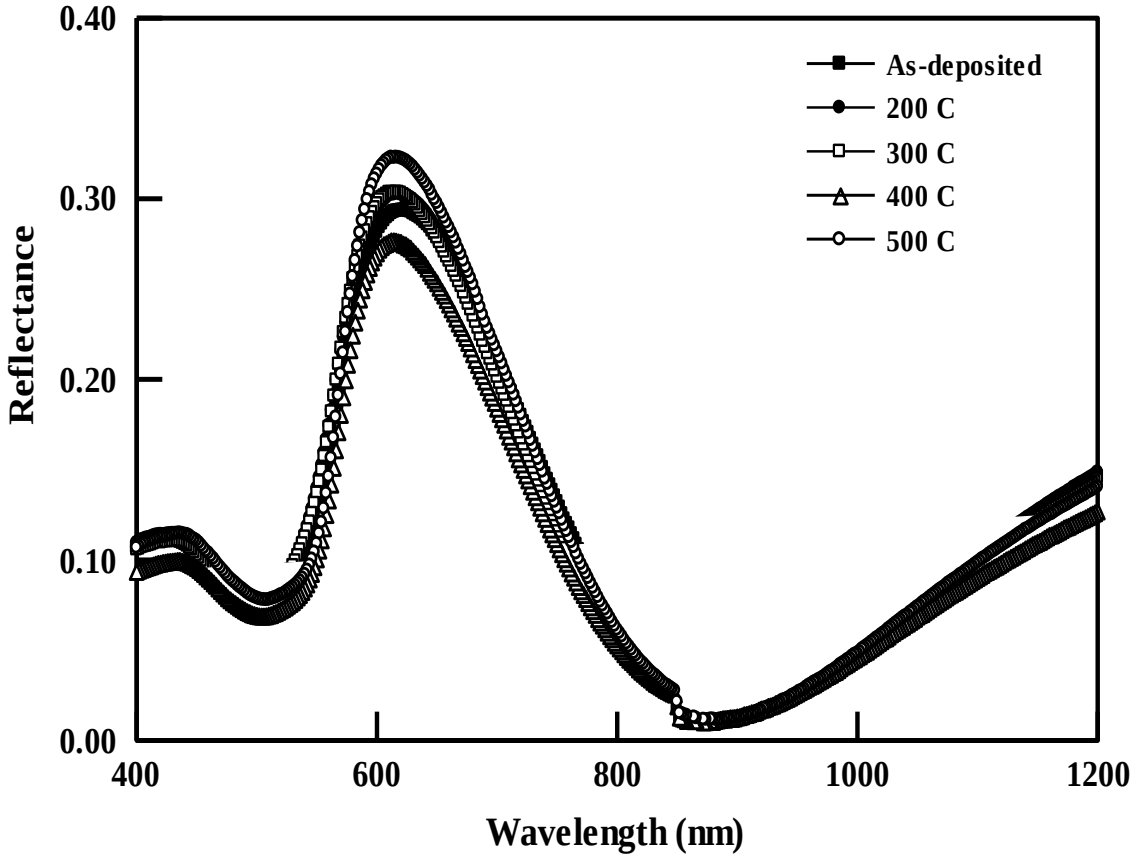

Figure 5.4. Measured normal-incidence reflectance spectra of the films deposited on unheated substrates in oxygen (RO films).

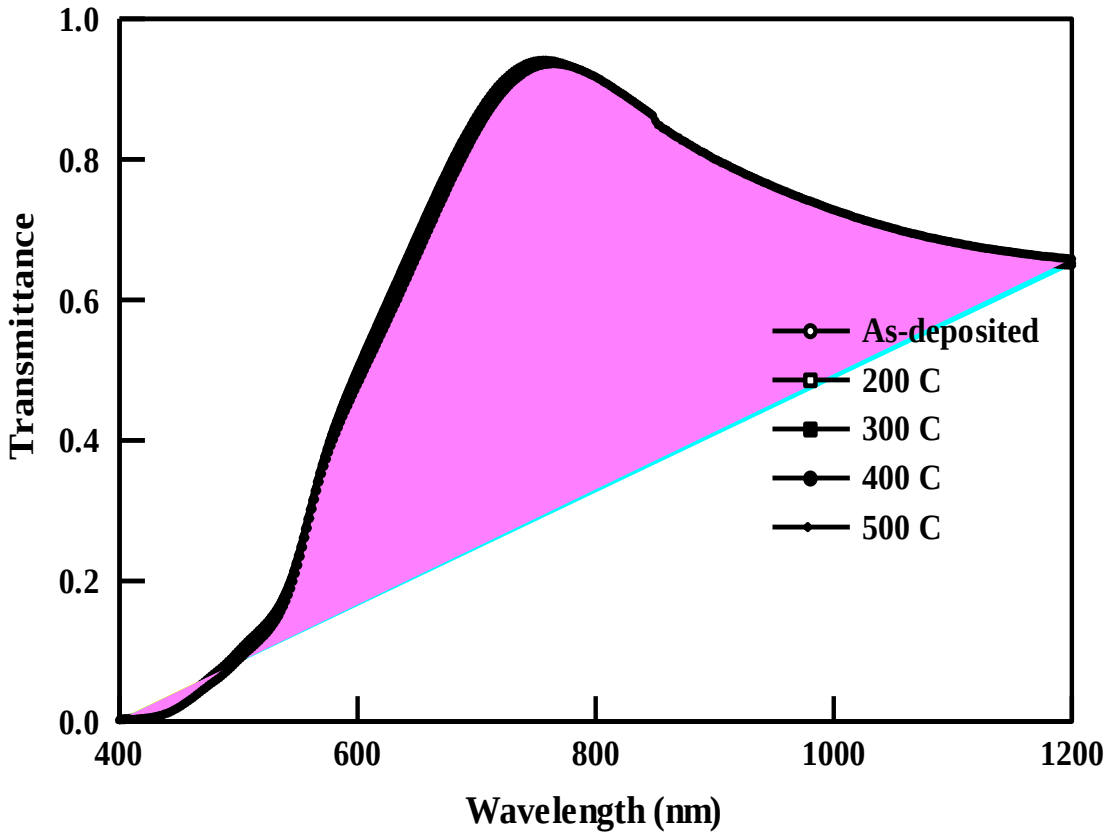

Figure 5.5. Measured normal-incidence transmittance spectra of the films deposited on heated substrates in oxygen (HO films).

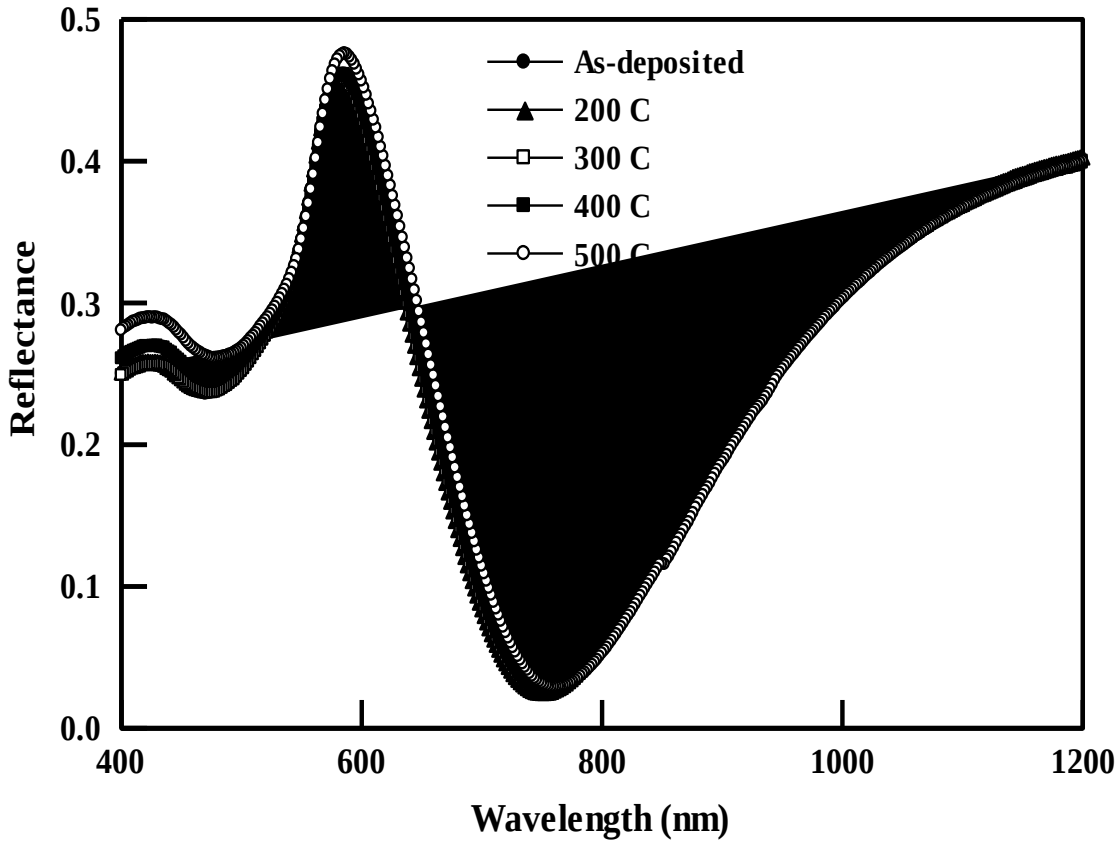

Figure 5.6. Measured normal-incidence reflectance spectra of the films deposited on heated substrates in oxygen (HO films).

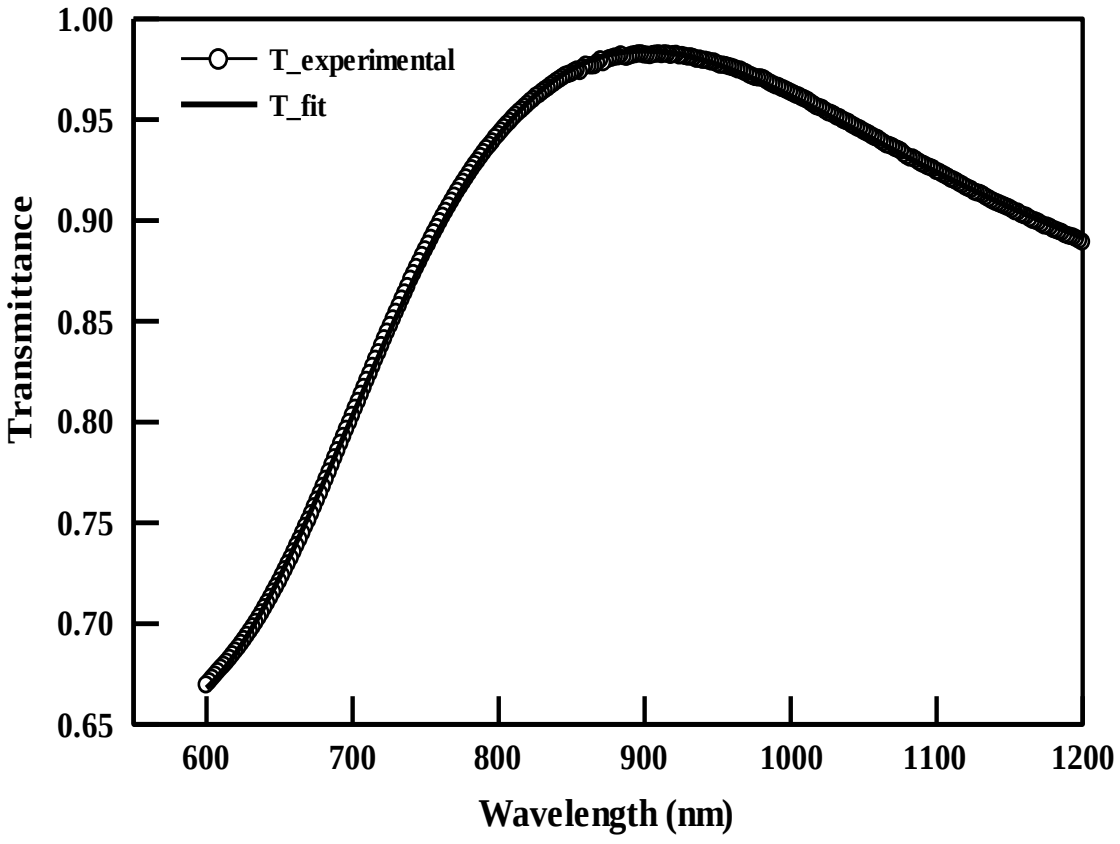

Figure 5.7. Fitting of the experimental transmittance spectrum of the film deposited on unheated substrate in oxygen (RO film) annealed at 200 ^{o}C by the model represented by equations 5.1 − 5.3.

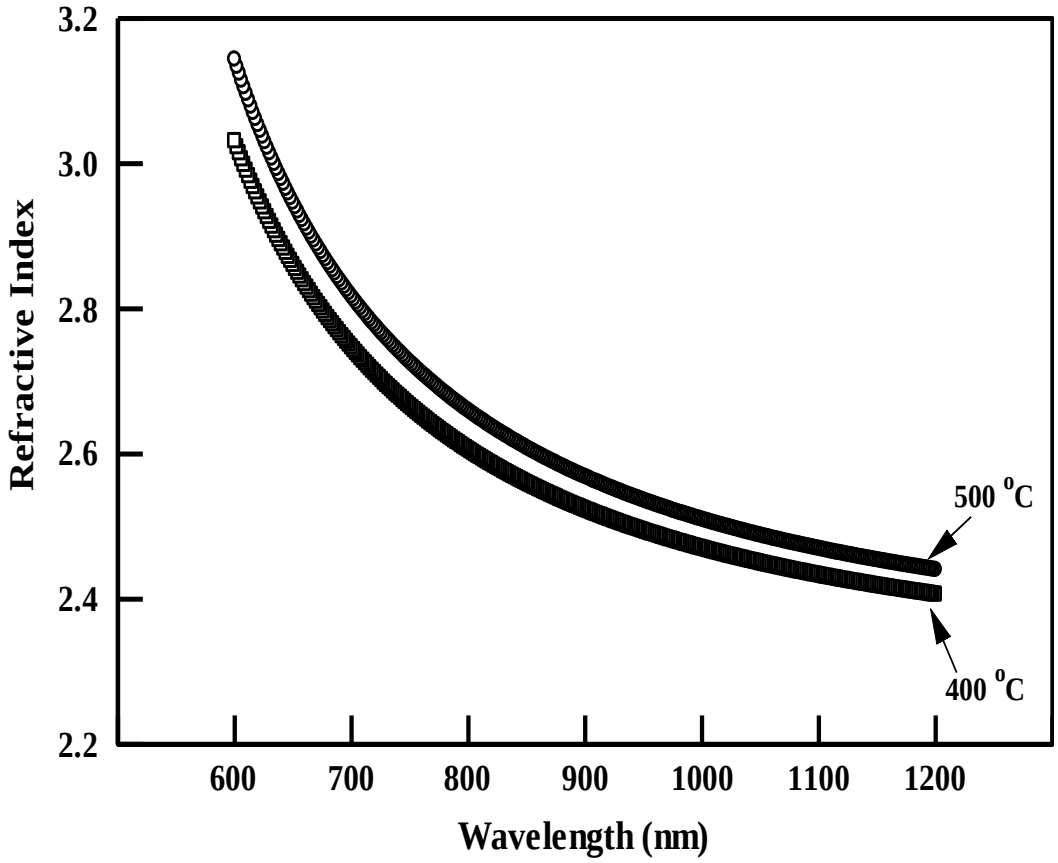

Figure 5.8. Variation of the refractive index of the films deposited on unheated substrates in vacuum (RW films) with the wavelength of light.

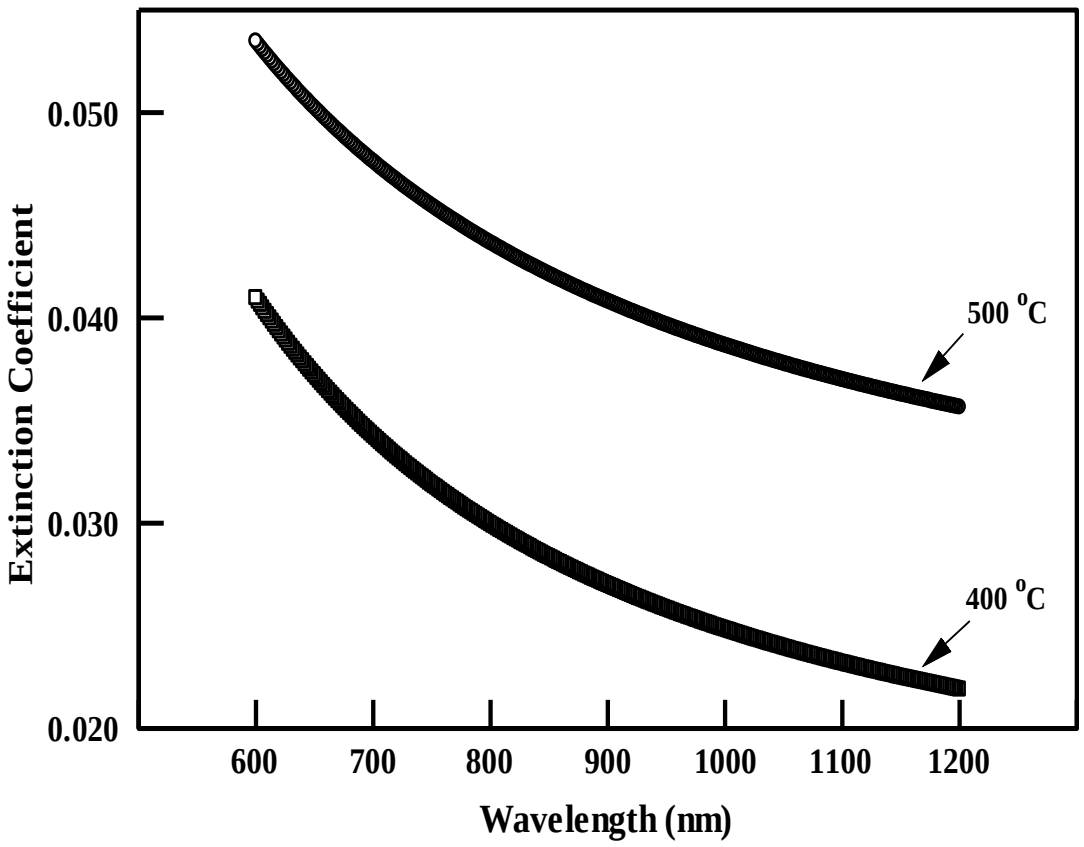

Figure 5.9. Variation of the extinction coefficient of the films deposited on unheated substrates in vacuum (RW films) with the wavelength of light.

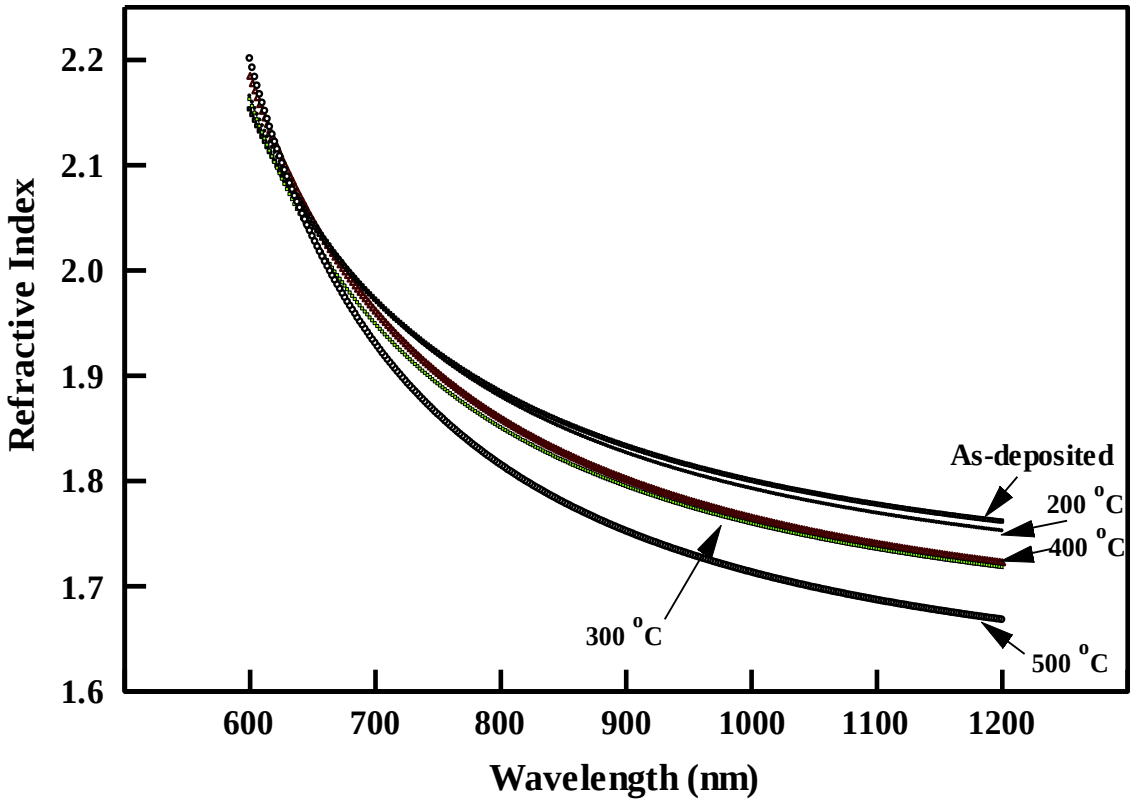

Figure 5.10. Variation of the refractive index of the films deposited on unheated substrates in oxygen (RO films) with the wavelength of light.

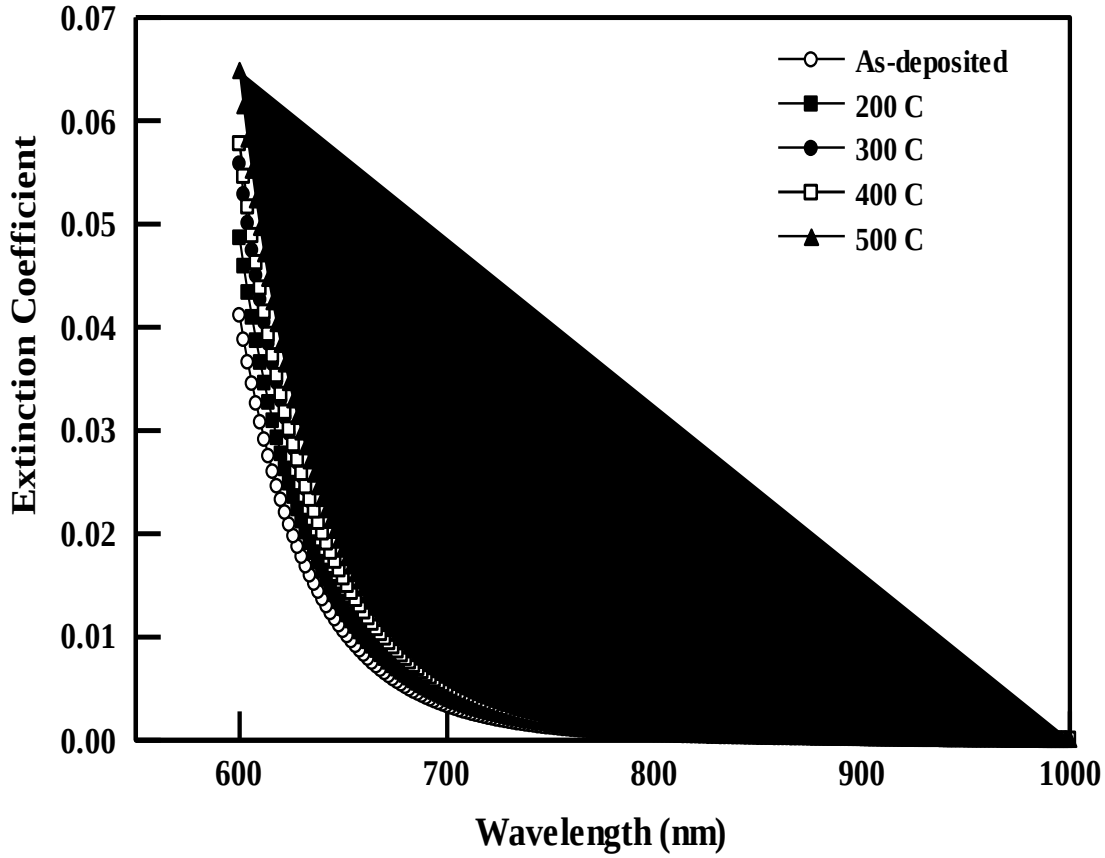

Figure 5.11. Variation of the extinction coefficient of the films deposited on unheated substrates in oxygen (RO films) with the wavelength of light.

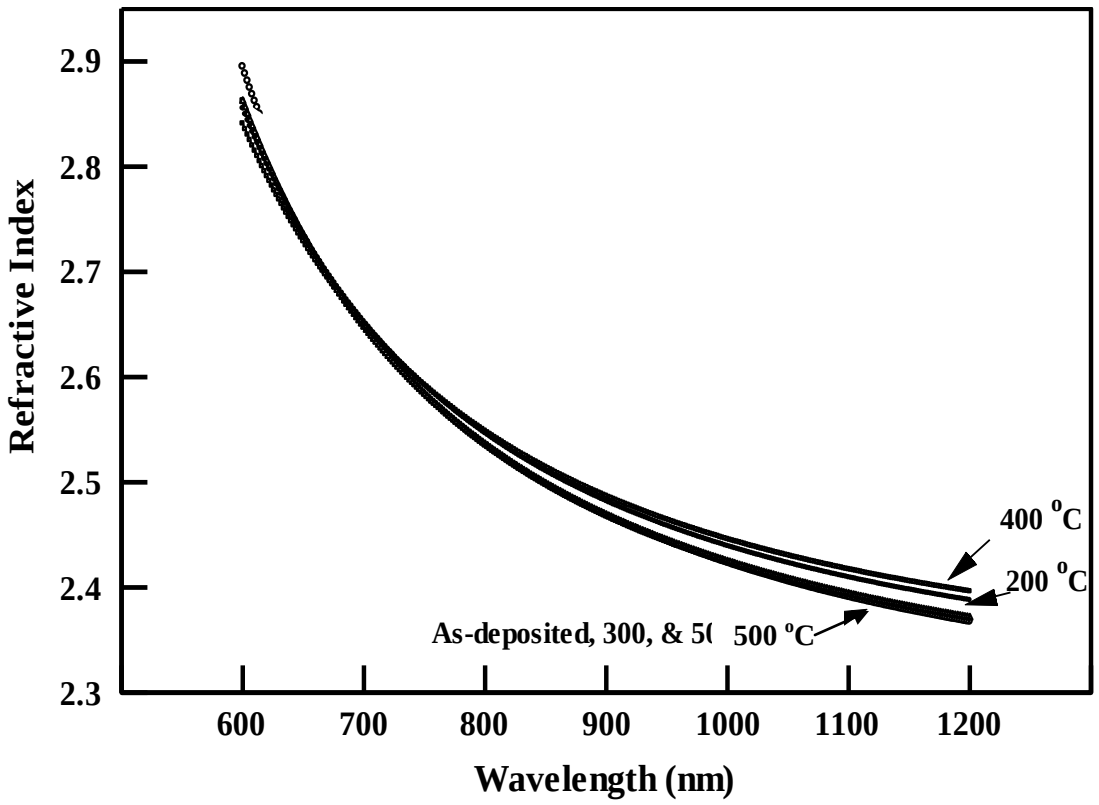

Figure 5.12. Variation of the refractive index of the films deposited on heated substrates in oxygen (HO films) with the wavelength of light.

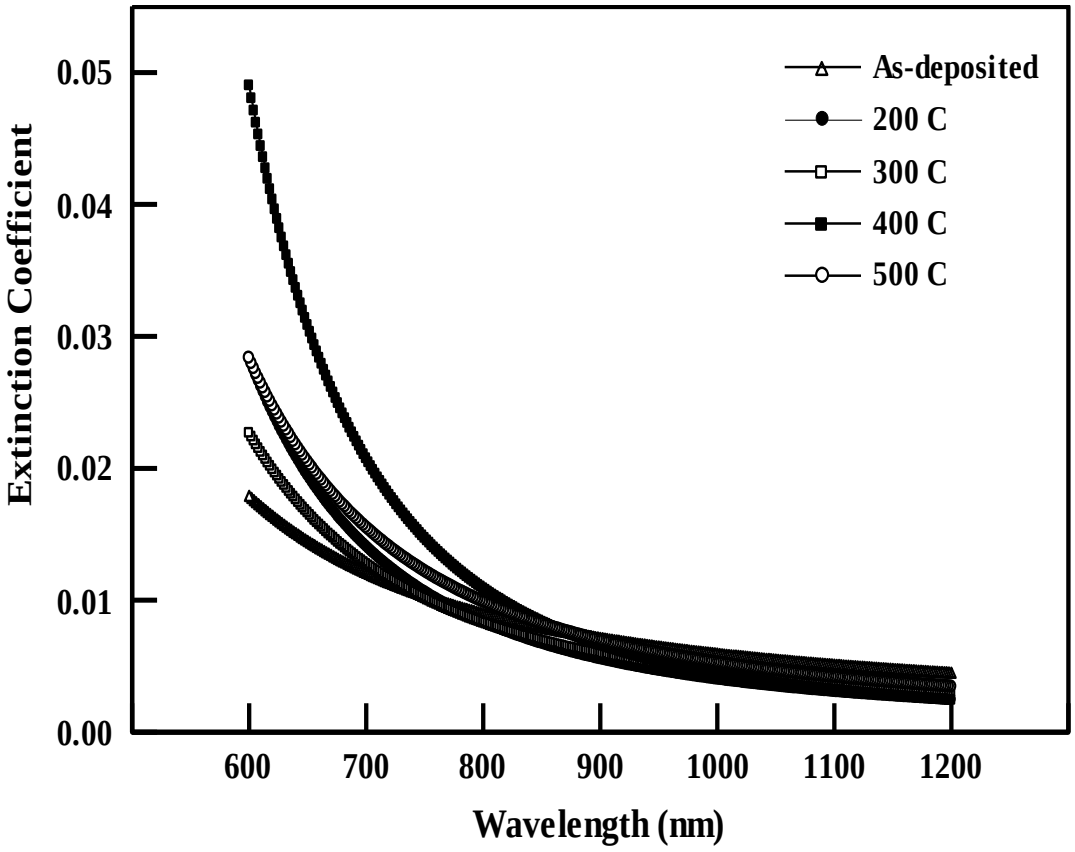

Figure 5.13. Variation of the extinction coefficient of the films deposited on heated substrates in oxygen (HO films) with the wavelength of light.

5.2 BAND GAP

The transmittance of a thin film can be written as [86]

$$T = \frac{(1-R)^2 \exp(-\alpha d)}{1-[R^2 \exp(-2\alpha d)]} \quad (5.5)$$

where R is the reflectance of the film. In the fundamental absorption region $\alpha > 10^4$ cm^{-1}, thus second term in the denominator of equation (5.5) is negligible. Therefore, equation (5.5) can be rewritten as

$$T = (1-R)^2 e^{(-\alpha d)} \quad (5.6)$$

Thus,

$$\alpha = \frac{1}{d} ln \left[\frac{(1-R)^2}{T}\right] \quad (5.7)$$

Figures 5.14, 5.15, and 5.16 show the absorption coefficient of RW, RO and HO films, respectively, calculated using equation (5.7). The absorption of RW films with annealing did not change until the photon energy exceeded 2.3 eV, where the absorbency features of films annealed at 500 ^{o}C were decreased as compare to films annealed at 400 ^{o}C. On the other hand the absorption of films was increased with increasing the photon energy (IR to UV region) for both RO and HO films. RO films also showed a small increment in absorption behavior with annealing temperatures, as can be seen in figure 5.15. However annealing did not affect the absorption of HO films.

In the absorption region, the absorption coefficient (α) and band gap (E_g) are related as [87]:

$$\alpha = \frac{\alpha_0}{E}\left(E - E_g\right)^{\eta} \quad (5.8)$$

where α_o is a constant with values between $10^5 - 10^6 cm^{-1}$ [87]. The constant η depends on the type of transitions involved: η = ½ corresponds to a direct allowed transition, and η = 2 corresponds to an indirect allowed transition. In order to obtain the band gap, $(\alpha E)^{1/\eta}$ is plotted as a function of photon energy. The linear portions of the curves are fitted using linear regression analysis. An extrapolation of the linear regions of the plots gives the value of the band gap as the intercept to the horizontal axis (where $\alpha E = 0$). Such plots are called Tauc plots and are shown in figure 5.17 for direct band gap and figure 5.18 for indirect band gap. The resulting band gap values are given in Table 5.2, where E_{gi} denotes the indirect band gap and E_{gd} denotes the direct band gap. It has been reported that α-Fe_2O_3 has an indirect band gap [88,89] as well as a direct band gap [82]. The reported values of the indirect band gap was in the range 1.38 eV to 2.09 eV [21,69,88–91]. On the other hand, the reported values of the direct band gap were in the range 1.95 eV to 2.35 eV [21,82,90,91]. We found the direct band gap and indirect band gap of all films to be 2.21±0.03 eV and 1.98±0.02 eV respectively, which are very well agree with the reported values. The value of direct and indirect band gaps of semiconductors can vary depending on the experimental conditions and variation in microstructure. The increase of the indirect band gap with substrate temperature was also reported for sprayed α-Fe_2O_3 thin films [91], although the opposite trend was reported for sputtered films [21]. However, we did not find substantial variation in direct as well as indirect band gaps because of annealing and substrate temperature.

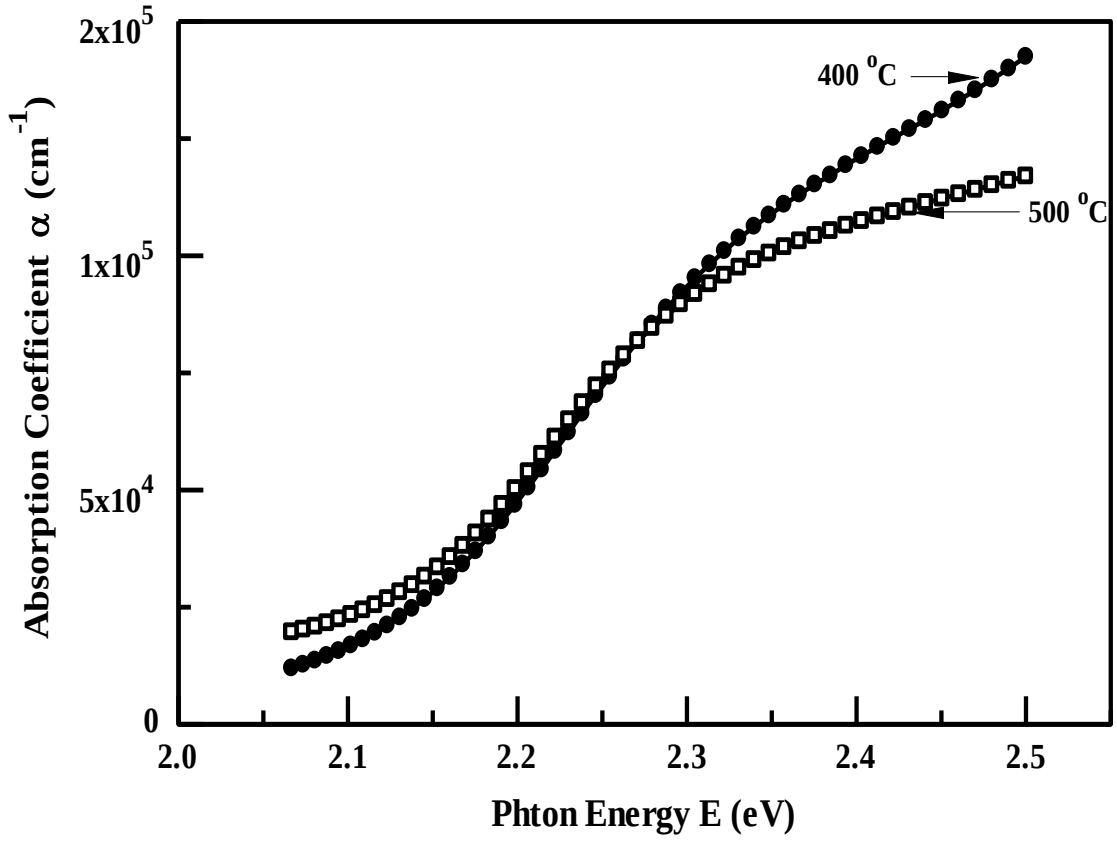

Figure 5.14. Dependence of the absorption coefficient of the films deposited on unheated substrates in vacuum (RW films) on photon energy.

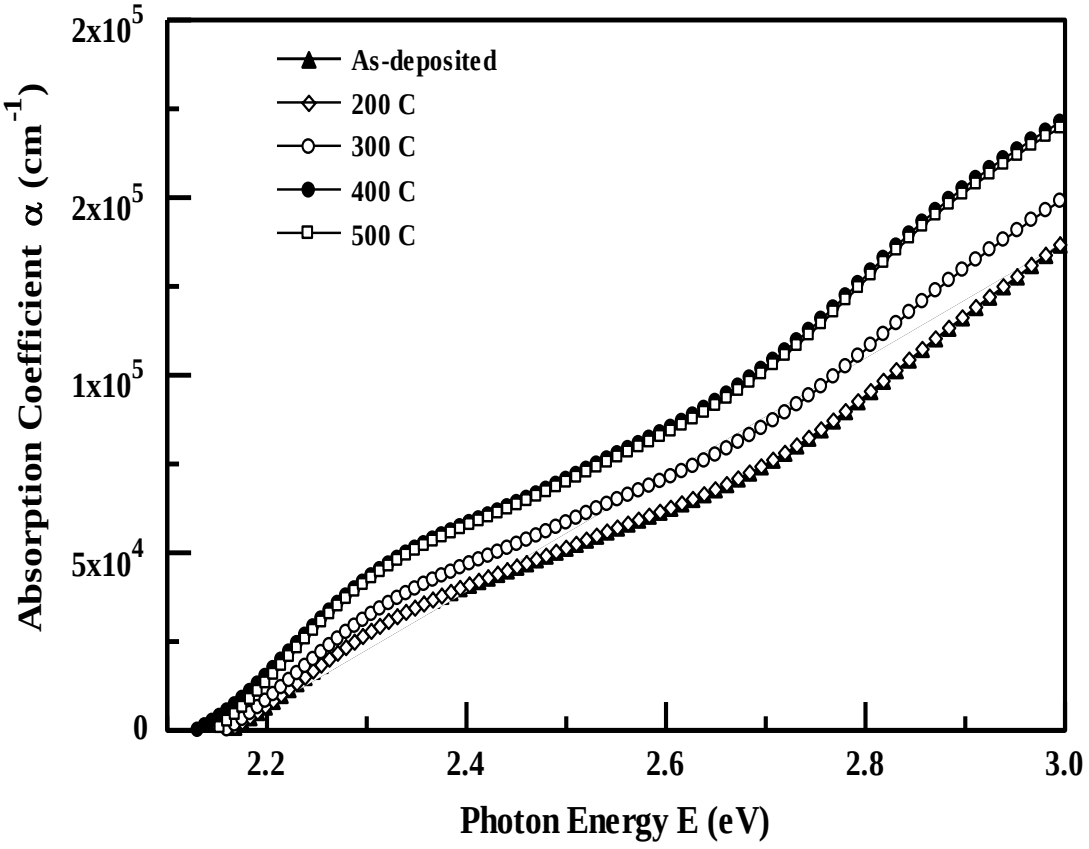

Figure 5.15. Dependence of the absorption coefficient of the films deposited on unheated substrates in oxygen (RO films) on photon energy.

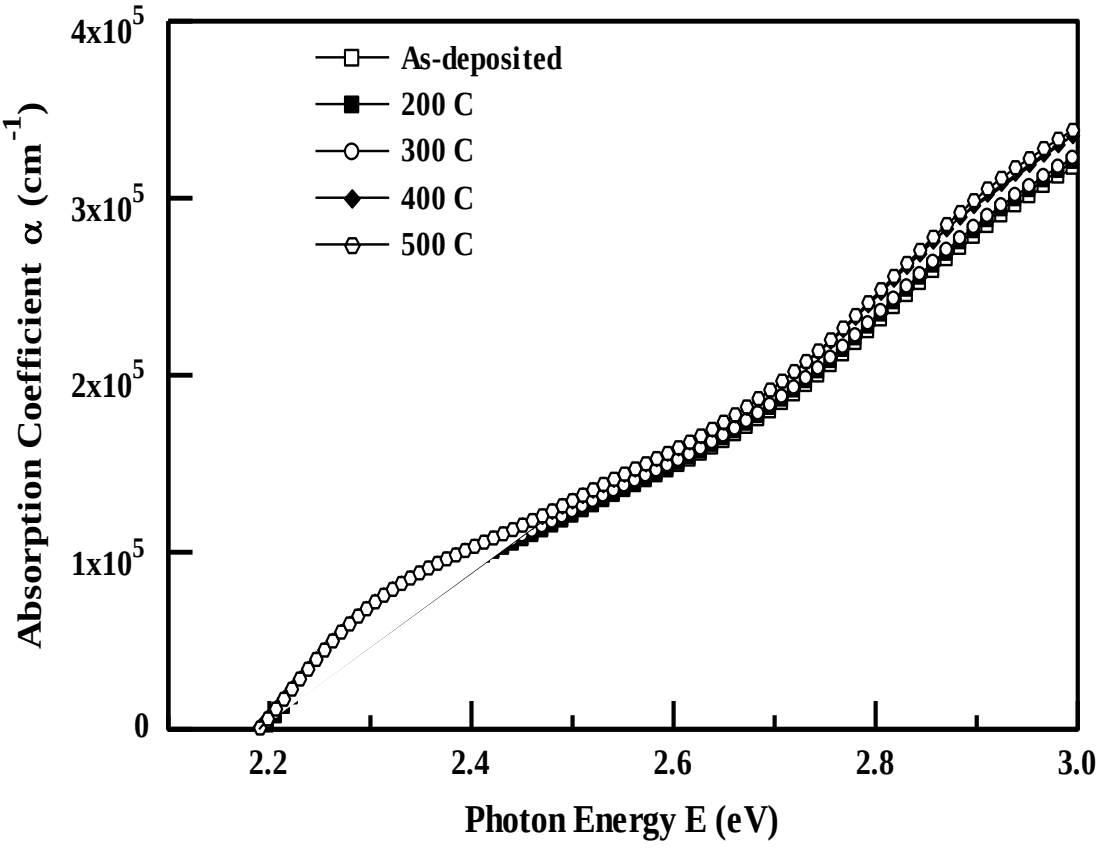

Figure 5.16. Dependence of the absorption coefficient of the films deposited on heated substrates in oxygen (HO films) on photon energy.

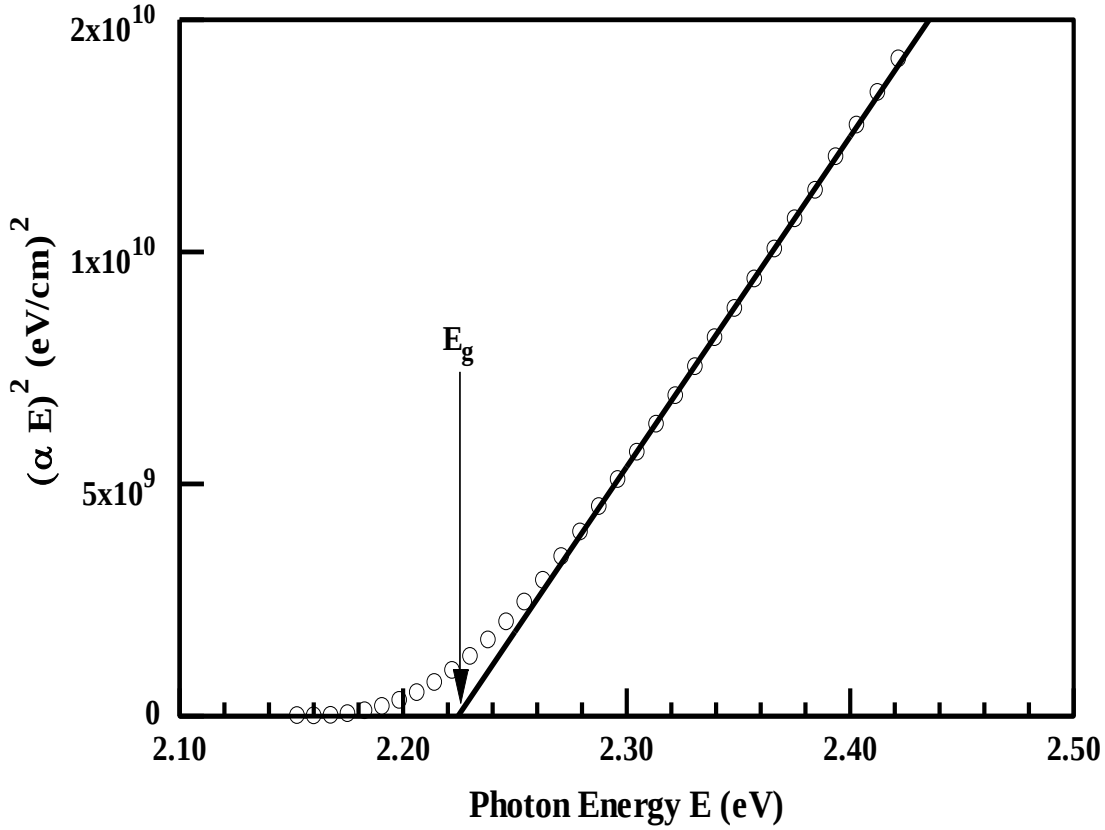

Figure 5.17. A representative Tauc plot of a film deposited on a unheated substrate in oxygen (RO film) and annealed at 300 ^{o}C, showing the direct band gap of the film.

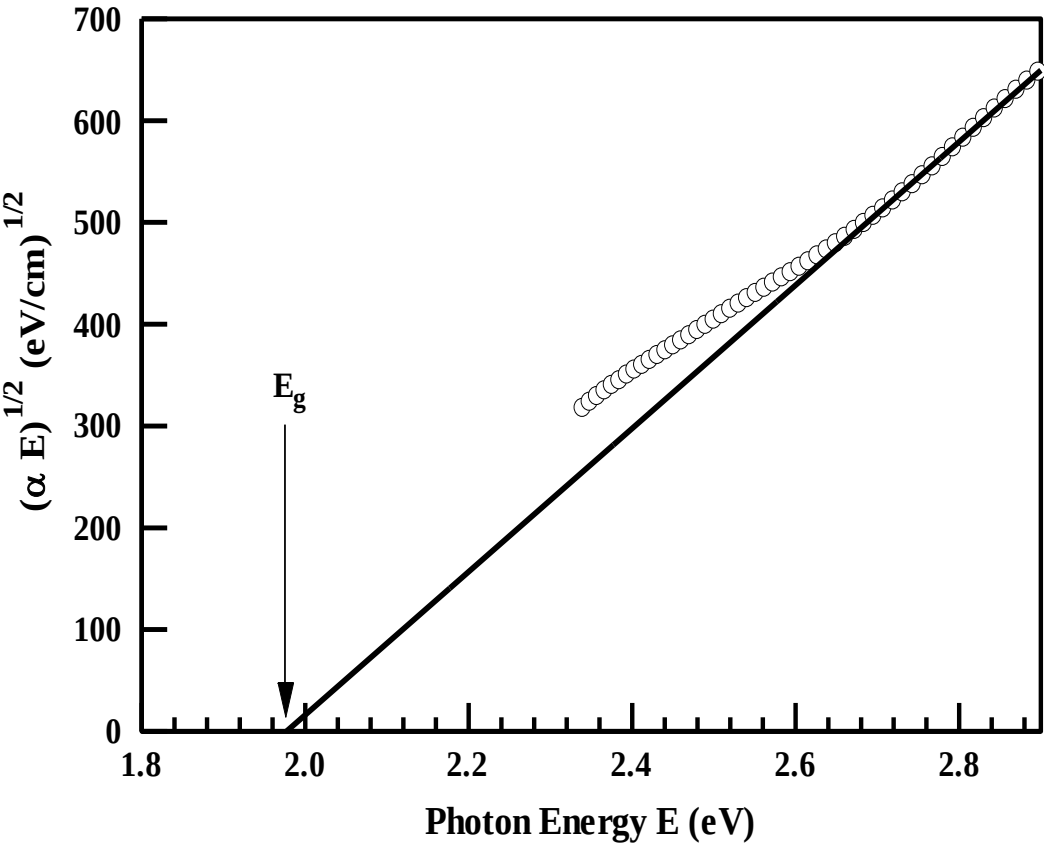

Figure 5.18. A representative Tauc plot of a film deposited on a unheated substrate in oxygen (RO film) and annealed at 300 ^{o}C, showing the indirect band gap of the film.

Table 5.2. The calculated values of direct and indirect band gaps.

Type	Annealing Temperature ^{o}C	E_{gi} (eV)	E_{gd} (eV)
RW films	400	2.0	2.18
	500	1.97	2.16
RO films	As-deposited	2.01	2.23
	200	2.00	2.24
	300	1.98	2.22
	400	1.95	2.20
	500	1.95	2.21
HO films	As-deposited	2.00	2.23
	200	2.01	2.23
	300	2.02	2.23
	400	2.00	2.23
	500	2.02	2.23

RW: films deposited on unheated substrates in vacuum, RO: films deposited on unheated substrates in oxygen, and HO: films deposited on heated substrates in oxygen.

CHAPTER 6

Conclusions and Future suggestions

6.1 CONCLUSIONS

In the present work, iron oxide thin films were fabricated by e-beam evaporation from pure iron. The effects of various experimental conditions, namely (i) deposition in vacuum and in oxygen ambient, (ii) deposition on heated and unheated substrates and, (iii) post annealing in range 200 ^{o}C – 500 ^{o}C were investigated. From the work, the following conclusions can be made.

- In case of films deposited in vacuum (RW films), α-Fe_2O_3 phase was obtained by post annealing the films at 400 ^{o}C and above.
- All the iron oxide films (α-Fe_2O_3) were polycrystalline with nano size crystallites.
- The post annealing mostly effect the films deposited in vacuum as compare to the films deposited in an oxygen ambient.
- The thickness of the films deposited in vacuum was changed from 113 nm to 229 nm by post annealing, but the thickness of the films deposited in an oxygen environment remained significantly unaffected.

- The films deposited in vacuum had larger values of surface roughness, which was found to increase with annealing temperature. The crystallite size and lateral grain size of the films was also increased with post deposition annealing.
- Although annealing did not influence the crystal size or surface roughness of the films deposited in oxygen (RO and HO films), it had a profound effect on the lateral grain size, where the largest grain size was obtained after annealing at 300 ^{o}C – 400 ^{o}C.
- Films deposited on heated substrates were more compact and denser as compared to the films deposited on unheated substrates
- XPS results indicated the presence of two oxide phases on the surfaces of the films, which is a reflection of the high reactivity of iron toward oxygen.
- The transparency of films deposited in vacuum was changed with annealing. However the transmittance was unaffected for the films deposited in oxygen on heated and unheated substrates.
- The films deposited on heated substrates had higher values of refractive index, as compared to the films deposited on unheated substrates in oxygen ambient.
- All The films exhibited direct and indirect band gaps. There was no substantial change either in direct band or in indirect band gaps of all the films with annealing as well as growth temperature.
- The main conclusion is that α-Fe_2O_3 thin films were prepared by the evaporation of pure iron. This represents a simple and economic method of obtaining these films.

6.2 SUGGESTIONS

1. Grow the iron oxide thin films directly from α-Fe_2O_3 target using e-beam evaporation and compare it with other techniques.
2. Investigate the magnetic properties of iron oxide films prepared by e-beam evaporation.
3. Investigate the photoluminescence of these films
4. Investigate the uses of these films in applications, such as:
    i. Gas sensing
    ii. Photovoltaics
    iii. Energy saving applications

REFERENCES

[1] R.M. Cornell, U. Schwertmann, The Iron Oxides: Structure, Properties, Reactions, Occurrences and Uses, 2nd ed., Wiley-VCH; 2nd, Completely Revised and Extended Edition edition (October 17, 2003), 2003.

[2] T. Stenberg, P. Vuoristo, J. Keranen, T. Mantyla, M. Buchler, S. Virtanen, et al., Characterization of rf sputtered iron oxide films for modeling passive films, 312 (n.d.) 46.

[3] B. Handke, J.B. Simonsen, M. Bech, Z. Li, P.J. Moller, Iron oxide thin film growth on Al2O3/NiAl(110), Surface Science. 600 (2006) 5123-5130.

[4] J.K. Kim, W.D. Moon, K.S. Lee, K.-hoon Jung, Formation of a highly oriented FeO thin film by phase transition of Fe 3 O 4 and Fe nanocrystallines, Thin Solid Films. 360 (2000) 118-121.

[5] Y. Peng, C. Park, D.E. Laughlin, Fe 3 O 4 thin films sputter deposited from iron oxide targets, Journal of Applied Physics. 93 (2003) 7957.

[6] W. Weiss, M. Ritter, Metal oxide heteroepitaxy: Stranski-Krastanov growth for iron oxides on Pt(111), Physical Review B. 59 (1999) 5201-5213.

[7] C. Pflitsch, D. Viefhaus, U. Bergmann, V. Kravets, H. Nienhaus, B. Atakan, Growth of Thin Iron Oxide Films on Si(100) by MOCVD, Journal of The Electrochemical Society. 153 (2006) C546.

[8] W. Eerenstein, L. Kalev, L. Niesen, T.T.M. Palstra, T. Hibma, Magneto-resistance and superparamagnetism in magnetite films on MgO and MgAl2O4, Journal of Magnetism and Magnetic Materials. 258-259 (2003) 73-76.

[9] H. Sawada, ELECTRON DENSITY STUDY OF SPINELS : MAGNESIUM CHROMIUM OXIDE, Materials Research Bulletin. 31 (1996) 361-366.

[10] T. Fujii, D. Alders, F.C. Voogt, T. Hibma, B.T. Thole, G.A. Sawatzky, In situ RHEED and XPS studies of epitaxial thin α-Fe 2 O 3 (0001) films on sapphire, Surface Science. 366 (1996) 579-586.

[11] L. Ferretto, A. Glisenti, Study of the surface acidity of an hematite powder, Journal of Molecular Catalysis. 187 (2002) 119-128.

[12] Y. Liu, D. Sun, Effect of CeO2 doping on catalytic activity of Fe2O3/gamma-Al2O(3) catalyst for catalytic wet peroxide oxidation of azo dyes., Journal of Hazardous Materials. 143 (2007) 448-54.

[13] H. Fu, X. Quan, H. Zhao, Photodegradation of γ-HCH by α-Fe2O3 and the influence of fulvic acid, Journal of Photochemistry and Photobiology A: Chemistry. 173 (2005) 143-149.

[14] E.L. Miller, R.E. Rocheleau, X.M. Deng, Design considerations for a hybrid amorphous silicon / photoelectrochemical multijunction cell for hydrogen production, International Journal of Hydrogen Energy. 28 (2003) 615-623.

[15] S.U.M. Khan, Z.Y. Zhou, Photoresponse of undoped and iodine-doped iron oxide thin film electrodes, Journal of Electroanalytical Chemistry. 357 (1993) 1-2.

[16] R. Tongpool, S. Jindasuwan, Sol–gel processed iron oxide–silica nanocomposite films as room-temperature humidity sensors, Sensors and Actuators B: Chemical. 106 (2005) 523-528.

[17] E.-T. Lee, G.-E. Jang, C.K. Kyo, D.-H. Yoon, Fabrication and gas sensing properties of α-Fe 2 O 3 thin film prepared by plasma enhanced chemical vapor deposition (PECVD), Sensors And Actuators. 77 (2001) 221-227.

[18] S.S. Shinde, R.A. Bansode, C.H. Bhosale, K.Y. Rajpure, Physical properties of hematite α-Fe 2 O 3 thin films: application to photoelectrochemical solar cells, Journal of Semiconductors. 32 (2011) 013001.

[19] A. Akl, Microstructure and electrical properties of iron oxide thin films deposited by spray pyrolysis, Applied Surface Science. 221 (2004) 319-329.

[20] S.S. Kulkarni, C.D. Lokhande, Structural, optical, electrical and dielectrical properties of electrosynthesized nanocrystalline iron oxide thin films, Materials Chemistry and Physics. 82 (2003) 151-156.

[21] E.L. Miller, D. Paluselli, B. Marsen, R.E. Rocheleau, Low-temperature reactively sputtered iron oxide for thin film devices, Thin Solid Films. 466 (2004) 307-313.

[22] Y.J. Park, K.M.A. Sobahan, C.K. Hwangbo, Optical and structural properties of Fe2O3 thin films prepared by ion-beam assisted deposition, Surface and Coatings Technology. 203 (2009) 2646-2650.

[23] X. Ye, D. Lin, Z. Jiao, L. Zhang, The thermal stability of nanocrystalline maghemite Fe 2 O 3, Journal of Physics D: Applied Physics. 2739 (1998).

[24] F. Jorgenson, The Complete Handbook of Magnetic Recording, 4th Editio, McGraw-Hill/TAB Electronics, 1995.

[25] C.B.D. Boer, M.J. Dekkers, Unusual thermomagnetic behaviour of haematites : neoformation of a highly magnetic spinel phase on heating in air, Geophysical Journal International. 144 (2001) 481-494.

[26] A.N. Shmakov, G.N. Kryukova, S.V. Tsybulya, A.L. Chuvilin, L.P. Solovyeva, Vacancy Ordering in γ-Fe 2 O 3 : Synchrotron X-ray Powder Diffraction and High-Resolution Electron Microscopy Studies, Journal of Applied Crystallography. 28 (1995) 141-145.

[27] L. Zhang, G.C. Papaefthymiou, J.Y. Ying, Size quantization and interfacial effects on a novel γ-Fe2]O3/SiO2 magnetic nanocomposite via sol-gel matrix-mediated synthesis, Journal of Applied Physics. 81 (1997) 6892.

[28] K. Siroky, J. Jiresova, L. Hudec, Iron oxide thin film gas sensor, Thin Solid Films. 245 (1994) 211-214.

[29] K. Kandori, I. Horii, A. Yasukawa, T. Ishikawa, Effects of surfactants on the precipitation and properties of colloidal particles from forced hydrolysis of FeCl3-HCl solution, Journal of Materials Science. 30 (1995) 41465.

[30] Y. Gao, Y.J. Kim, S. Thevuthasan, S. a. Chambers, P. Lubitz, Growth, structure, and magnetic properties of γ-Fe2O3 epitaxial films on MgO, Journal of Applied Physics. 81 (1997) 3253.

[31] D. Wiarda, T. Wenzel, HYPERFINE INTERACTION OF lllCd IMPURITIES IN Mn203, Mn3O4 AND B-Fe203, Journal of Physics and Chemistry of Solids. 53 (1992) 1199-1209.

[32] Y. Ikeda, M. Takano, Y. Barmo, Formation Mechanism of Neddle-Like alpha-Fe2O3 Particles Grown Along the c Axis and Characterization of Precursorily Formaed beta-Fe2O3, Bulletin of the Institute for Chemicalv Research, Kyoto University. 64 (1986) 249-258.

[33] E. Tronc, C. Chaneac, J.P. Jolivet, Structural and Magnetic Characterization of E-Fe 2 O 3, 104 (1998) 93-104.

[34] R.N. Goyal, D. Kaur, A.K. Pandey, Growth and characterization of iron oxide nanocrystalline thin films via low-cost ultrasonic spray pyrolysis, Materials Chemistry and Physics. 116 (2009) 638-644.

[35] B. Ouertani, J. Ouerfelli, M. Saadoun, H. Ezzaouia, B. Bessais, Characterisation of iron oxide thin films prepared from spray pyrolysis of iron trichloride-based aqueous solution, Thin Solid Films. 516 (2008) 8584-8586.

[36] K. Shalini, G.N. Subbanna, S. Chandrasekaran, S.A. Shivashankar, Thin films of iron oxide by low pressure MOCVD using a novel precursor : tris (t-butyl-3-oxo-butanoato) iron (III), Thin Solid Films. 424 (2003) 56-60.

[37] M.K. Singh, Y. Yang, C.G. Takoudis, Low-Pressure Metallorganic Chemical Vapor Deposition of Fe2O3 Thin Films on Si(100) Using n-Butylferrocene and Oxygen, Journal of The Electrochemical Society. 155 (2008) 618-623.

[38] T. Tepper, C.A. Ross, G.F. Dionne, Microstructure and Optical Properties of Pulsed-Laser-Deposited Iron Oxide Films, Ieee Transactions on Magnetics. 40 (2004) 1685-1690.

[39] M. Ouyang, H. Hiraoka, Preparation and characterization of iron oxide films by the excimer laser ablation of poly (ferric methacrylate), Materials Science Engineering B. 34 (1995) 188-191.

[40] M. Shima, T. Tepper, C.A. Ross, Magnetic properties of chromium oxide and iron oxide films produced by pulsed laser deposition, Journal of Applied Physics. 91 (2002) 7920.

[41] C. Ruby, B. Humbert, J. Fusy, Surface and interface properties of epitaxial iron oxide thin films deposited on MgO (001) studied by XPS and Raman spectroscopy, Surface And Interface Analysis. 380 (2000) 377-380.

[42] M. Hasegawa, H. Yanagihara, Y. Toyoda, E. Kita, L. Ranno, Electrical and magnetic properties of γ-Fe2O3 epitaxial films, Journal of Magnetism and Magnetic Materials. 310 (2007) 2283-2285.

[43] G. Waddill, O. Ozturk, Epitaxial growth of iron oxide films on Ag(111), Surface Science. 575 (2005) 35-50.

[44] M. Aronniemi, J. Lahtinen, P. Hautojärvi, Characterization of iron oxide thin films, Surface and Interface Analysis. 36 (2004) 1004-1006.

[45] J.S. Corneille, J.-W. He, D.W. Goodman, Preparation and characterization of ultra-thin iron oxide films on a Mo (100) surface, Surface Science. 338 (1995) 211-224.

[46] T. Fujii, M. Takano, R. Katano, Y. Bando, Preparation and characterization of (111)-oriented Fe3O4 films deposited on sapphire, Journal of Applied Physics. 66 (1989) 3168-3172.

[47] M. Chiba, K. Morio, Y. Koizumi, Microstructure and magnetic properties of iron oxide thin films by solid reaction, Journal of Magnetism and Magnetic Materials. 239 (2002) 457-460.

[48] S. Jain, A.O. Adeyeye, S.Y. Chan, C.B. Boothroyd, Interface properties of iron oxide films, Journal of Physics D: Applied Physics. 37 (2004) 2720-2725.

[49] C. Ruby, J. Fusy, J.R. Ge, Â.H. Poincare, Preparation and characterization of iron oxide films deposited on MgO (100), Thin Solid Films. 352 (1999) 22-28.

[50] L. Eckertova, Physics of Thin Films, 2nd editio, Springer, 1984.

[51] M. Ohring, The Materials Science of Thin Films, Academic Press Limited, 1992.

[52] N.W. Ashceoft, N.D. Mermin, Solid State Physics, Brooks/Cole Cengage Learning, 1976.

[53] http://en.wikipedia.org/wiki/Atomic_Force_Microscopy, (n.d.).

[54] D. Briggs, M.P. Seah, Practical Surface Analysis by Auger and X-ray Photoelectron Spectroscopy, John Wiley & Sons Ltd, 1983.

[55] ICDD files: (01-087-0722) for elemental iron; (01-071-5088) for α-Fe2O3., (n.d.).

[56] P. Singh, A. Kumar, Deepak, D. Kaur, Growth and characterization of ZnO nanocrystalline thin films and nanopowder via low-cost ultrasonic spray pyrolysis, Journal of Crystal Growth. 306 (2007) 303-310.

[57] C. Suryanarayana, M. Grant Norton, X-Ray Diffraction A Practical Approach, Plenum Press, New York, 1998.

[58] B.-Z. Dong, G.-J. Fang, J.-F. Wang, W.-J. Guan, X.-Z. Zhao, Effect of thickness on structural, electrical, and optical properties of ZnO: Al films deposited by pulsed laser deposition, Journal of Applied Physics. 101 (2007) 033713.

[59] E. Centinorgu, S. Goldsmith, Y. Rosenberg, R.L. Boxman, Influence of annealing on the physical properties of filtered vacuum arc deposited tin oxide thin films, Journal of Non-Crystalline Solids. 353 (2007) 2595-2602.

[60] J.A. Thornton, High Rate Thick Film Growth, Annual Review of Materials Science. 7 (1977) 239-260.

[61] C.S. Kuivila, J.B. Butt, P.C. Stair, Characterization of surface species on iron synthesis catalysts by X-ray photoelectron spectroscopy, Applied Surface Science. 32 (1988) 99-121.

[62] V. Stambouli, C. Palacio, H.J. Mathieu, D. Landolt, Comparison of in-situ low-pressure oxidation of pure iron at room temperature in 0 2 and in O 2/ H 2 O mixtures using XPS, Applied Surface Science. 70/71 (1993) 240-244.

[63] P. Graat, M.A.J. Somers, Quantitative Analysis of Overlapping XPS Peaks by Spectrum Reconstruction : Determination of the Thickness and Composition of Thin Iron Oxide Films ", Surface and Interface Analysis. 26 (1998) 773-782.

[64] Y. Gao, Y.J. Kim, S.A. Chambers, G. Bai, Synthesis of epitaxial films of Fe3O4 and α-Fe2O3 with various low-index orientations by oxygen-plasma-assisted molecular beam epitaxy, 332 (1997).

[65] G.H. Vurens, M. Salmeron, G.A. Somorjai, Structure, composition and chemisorption studies of thin ordered iron oxide films on platinum (111), Surface Science. 201 (1988) 129-144.

[66] T. Schedel-Niedeig, W. Weiss, R. Schlogl, Electronic structure of ultrathin ordered iron oxide films grown onto Pt(111), Physical Review B. 52 (1995) 17449.

[67] T. Fujii, F.M.F.D. Groot, G.A. Sawatzky, F.C. Voogt, T. Hibma, K. Okada, In situ XPS analysis of various iron oxide films grown by NO 2 -assisted molecular-beam epitaxy, Physical Review B. 59 (1999) 3195-3202.

[68] F. Yubero, A.R. Gonzalez, S. Tougaard, Determination of growth mechanisms by X-ray photoemission and ion scattering spectroscopies : application to thin iron oxide films deposited on SiO2, Surface Science. 457 (2000) 24-36.

[69] L. Dghoughi, B. Elidrissi, C. Bernede, M. Assou, M. Lamrani, M. Regragui, et al., Physico-chemical, optical and electrochemical properties of iron oxide thin films prepared by spray pyrolysis, Applied Surface Science. 253 (2006) 1823-1829.

[70] T.Y. Ma, I.C. Lee, Influence of substrate temperature on the structural and electrical properties of α-Fe2O3 films prepared by ultrasonic spray pyrolysis, Journal of Materials Science: Materials in Electronics. 15 (2004) 775–780.

[71] O.S. Heavens, Optical Properties of Thin Solid Films, Dover Publications, 1991.

[72] J.C. Manifacier, J. Gasiot, J.P. Fillard, A simple method for the determination of the optical constants n, k and the thickness of a weakly absorbing thin film, Journal of Physics E. 9 (1976) 1002-1004.

[73] S.H. Wemple, M. Didomenico, Behavior of the Electronic Dielectric Constant in Covalent and Ionic Materials, Physical Review B. 3 (1971) 1338-1351.

[74] S. Zhao, F. Ma, K.W. Xu, H.F. Liang, Optical properties and structural characterization of bias sputtered ZrO2 films, Journal of Alloys and Compounds. 453 (2008) 453-457.

[75] G. Girtan, M, Folcher, Structural and optical properties of indium oxide thin films prepared by an ultrasonic spray CVD process, Surface and Coatings Technology. 172 (2003) 242-250.

[76] I.H. Malitson, Interspecimen Comparison of the Refractive Index of Fused Silica, Journal of the Optical Society of America. 55 (1965).

[77] K. Morl, U. Ropke, B. Knappe, J. Lehmann, R. Perthel, H. Schrodek, Optical properties of sputtered Fe203 films, Thin Solid Films. 60 (1979) 49-53.

[78] A.A. Akl, Influence of preparation conditions on the dispersion parameters of sprayed iron oxide thin films, Applied Surface Science. 256 (2010) 7496-7503.

[79] R. Thielsch, A. Gatto, J. Heber, N. Kaiser, A comparative study of the UV optical and structural properties of SiO2 , Al2O3 , and HfO2 single layers deposited by reactive evaporation , ion- assisted deposition and plasma ion-assisted deposition, Thin Solid Films. 410 (2002) 86-93.

[80] H. Hu, C. Zhu, Y.F. Lu, Y.H. Wu, T. Liew, M.F. Li, et al., Physical and electrical characterization of HfO2 metal–insulator–metal capacitors for Si analog circuit applications, Journal of Applied Physics. 94 (2003) 551.

[81] T. Tan, Z. Liu, H. Lu, W. Liu, H. Tian, Structure and optical properties of HfO2 thin films on silicon after rapid thermal annealing, Optical Materials. 32 (2010) 432-435.

[82] M. Gartner, M. Crisan, A. Jitianu, R. Scurtu, R. Gavrila, I. Oprea, et al., Spectroellipsometric Characterization of Multilayer Sol-Gel Fe 2 O 3 Films, Journal of Sol-Gel Science and Technology. 3 (2003) 745-748.

[83] M. Harris, H.A. Macleod, S. Ogura, The relationship between optical inhomogeneity and film strucutre, Thin Solid Films. (1978) 173-178.

[84] I.N. Sokolik, O.B. Toon, Incorporation of mineralogical composition into models of the radiative properties of mineral aerosol from UV to IR wavelengths, Journal of Geophysical Research. 104 (1999) 9423-9444.

[85] K. Sangwal, W. Kucharczyk, Relationship between density and refractive index of inorganic solids, Journal of Physics D: Applied Physics. 20 (1987) 522-525.

[86] J.I. Pankove, Optical Processes in Semiconductors, Dover Publications, 1971.

[87] Y. Natsume, H. Sakata, Electrical and optical properties of zinc oxide films post-annealed in H2 after fabrication by sol – gel process, Materials Chemistry and Physics. 78 (2002) 170-176.

[88] N. Ozer, F. Tepehan, Optical and electrochemical characteristics of sol — gel deposited iron oxide films, Solar Energy Materials and Solar Cells. 56 (1999) 141-152.

[89] G. Zotti, G. Schiavon, S. Zecchin, U. Casellato, Electrodeposition of Amorphous Fe203 Films by Reduction of Iron Perchiorate in Acetonitrile, The Electrochemical Society. 145 (1998) 385-389.

[90] N. Beermann, L. Vayssieres, S.-eric Lindquist, A. Hagfeldt, Photoelectrochemical Studies of Oriented Nanorod Thin Films of Hematite, Current. 147 (2000) 2456-2461.

[91] A.A. Akl, Optical properties of crystalline and non-crystalline iron oxide thin films deposited by spray pyrolysis, Applied Surface Science. 233 (2004) 307-319.

VITA

Name : Muhammad Saleem

E-mail: saleem.ph@gmail.com, saleem_ph@yahoo.com

Nationality: Pakistani

Education

1. M.S Physics (Master of Science), 2012, Department of Physics, King Fahd University of Petroleum & Minerals (KFUPM), Dhahran, Saudi Arabia.
2. M.Sc Physics (Master of Science), 2006, Department of Physics, University of Peshawar, Pakistan.
3. B.Sc (Bachelor of Science), 2004, Hazara University, Mansehra, Pakistan

Experience

1. ***Research Assistant*** (2009 − 2012) Department of Physics, King Fahd University of Petroleum & Minerals (KFUPM), Dhahran, Saudi Arabia.
2. ***Lecturer*** (2007 − 2009) Physics Department, COMSATS Institute of Information Technology (CIIT) Islamabad, Pakistan.

Publications

1. M.F. Al-Kuhaili, **M. Saleem**, S.M.A. Durrani, Optical properties of iron oxide (α-Fe2O3) thin films deposited by the reactive evaporation of iron, Journal of Alloys and Compounds, 521 (2012).
2. **M. Saleem**, M.F. Al Kuhaili, S.M.A. Durrani, I.A. Bakhtiari, Characterization of nanocrystalline α-Fe2O3 thin films grown by reactive evaporation and oxidation of iron, Physica Scripta. 85 (2012).